

# TriQXNet: Forecasting Dst Index from Solar Wind Data Using an Interpretable Parallel Classical–Quantum Framework with Uncertainty Quantification

Md Abrar Jahin<sup>1,6</sup>, M. F. Mridha<sup>2,\*</sup>, Zeyar Aung<sup>3</sup>, Nilanjan Dey<sup>4</sup>, and R. Simon Sherratt<sup>5</sup>

<sup>1</sup>Department of Industrial Engineering and Management, Khulna University of Engineering & Technology (KUET), Khulna, 9203, Bangladesh

<sup>2</sup>Department of Computer Science, American International University-Bangladesh, Dhaka, 1229, Bangladesh

<sup>3</sup>Center for Secure Cyber-Physical Systems (C2PS) and Department of Computer Science, Khalifa University, Abu Dhabi, 127788, UAE

<sup>4</sup>Department of Computer Science & Engineering, Techno International New Town, New Town, Kolkata, India

<sup>5</sup>Department of Biomedical Engineering, University of Reading, UK

<sup>6</sup>Physics and Biology Unit, Okinawa Institute of Science and Technology Graduate University (OIST), Okinawa, 904-0412, Japan

\*Corresponding author: M. F. Mridha (e-mail: firoz.mridha@aiub.edu).

## ABSTRACT

Geomagnetic storms, which are brought on by the transmission of solar wind energy to the Earth's magnetic field, have the potential to substantially damage a number of critical infrastructure systems, including GPS, satellite communications, and electrical power grids. The disturbance storm-time (Dst) index is used to determine how strong these storms are. Using real-time solar wind data, a variety of models—empirical, physics-based, and machine-learning—have improved Dst forecasting during the last thirty years. However, forecasting extreme geomagnetic events is still difficult, requiring reliable ways to manage unprocessed, real-time data streams in the face of noise and sensor failures. This research aims to create a Dst forecasting model that employs specific real-time solar wind data feeds, functions under realistic restrictions, and outperforms state-of-the-art models in terms of prediction. Innovative methods are needed to solve this complex challenge, as it is not immediately evident what the optimal solution is. This study introduces a groundbreaking application of quantum computing in space weather forecasting. Our novel framework represents a pioneering integration of classical and quantum computing, conformal prediction, and explainable AI (XAI) within a hybrid neural network architecture. To ensure high-quality input data, we developed a comprehensive data preprocessing pipeline that includes feature selection, normalization, aggregation, and imputation. The hybrid classical–quantum neural network, TriQXNet, leverages three parallel channels to process preprocessed solar wind data, significantly enhancing the robustness and accuracy of Dst index predictions. Our model predicts the Dst index using solar wind measurements from NASA's ACE and NOAA's DSCOVR satellites for the hour that is currently underway ( $t_0$ ) as well as the hour that will follow ( $t_{+1}$ ), providing vital advance notice to lessen the negative consequences of geomagnetic storms. TriQXNet outperforms 13 state-of-the-art hybrid deep-learning models, achieving a root mean squared error of 9.27 nanoteslas (nT). Rigorous evaluation through 10-fold cross-validated paired t-tests confirmed TriQXNet's superior performance with 95% confidence. By implementing conformal prediction techniques, we provide quantifiable uncertainty in our forecasts, which is essential for operational decision-making. Additionally, incorporating XAI methods such as ShapTime and permutation feature importance enhances the interpretability of the model, fostering greater trust in its predictions. Comparative analysis revealed that TriQXNet outperforms existing models in the literature and the model deployed by the CIRES/NCEI geomagnetism team. Our model demonstrated exceptional forecasting accuracy for dual hours in a specific case study involving rapid Dst value decline. This research sets a new level of expectations for geomagnetic storm forecasting, showing the potential of classical–quantum hybrid models to improve space weather prediction capabilities.

## Introduction

Geomagnetic storms, principally induced by coronal mass ejections and co-rotating interaction areas, represent an imminent threat to modern technological systems as they may cause catastrophic disruptions of power grids, GPS navigation, and satellite communications<sup>1</sup>. The Earth's magnetic field, due to the effective coupling of amplified solar wind with the ground magnetic field, leads to significant errors in systems using it as a pointing reference. These fluctuations can disrupt the accuracy of

compasses, magnetometers, and other devices that rely on magnetic field measurements for navigation or orientation. It is important for users of these systems to be aware of potential errors during periods of heightened solar activity. An essential indicator in this regard is the disturbance storm time (Dst)<sup>2</sup> index, which gauges the intensity of geomagnetic storms. The Dst index is a standardized indicator of geomagnetic disturbances and is computed using data from four near-equatorial observatories (San Juan, Honolulu, Kakioka, and Hermanus)<sup>3</sup>. Its values, which come from the magnetic field's horizontal component, are vital for powering geomagnetic models such as the NOAA/NCEI High Definition Geomagnetic Model—Real Time (HDGM-RT)<sup>4–8</sup>. This model provides high-resolution geomagnetic field predictions that are essential for a variety of applications, such as directional drilling and satellite operations. Based on measurements from four geomagnetic observatories, the intensity of these geomagnetic storms is determined by Dst, which is represented in nanoteslas. Lower Dst readings indicate a weakening of the Earth's magnetic field, a phenomenon associated with geomagnetic storms. Storms are classified as moderate when the Dst reading falls  $> -50$  nanoteslas (nT). Readings between  $-50 \leq Dst \leq -250$  nT signify an intense storm. If the Dst value plunges below  $< -250$  nT, the storm is considered a super-storm<sup>9</sup>.

Many techniques have emerged to model and forecast the Dst index. One such approach, proposed by Burton et al.<sup>10</sup>, utilizes differential equations to create a Dst index model. This model incorporates solar wind parameters as the driving force within the equations. Using a time-delayed artificial neural network (ANN), Gleisner et al.<sup>11</sup> led the way in developing Dst prediction models. Their model, which is based on solar wind data, anticipates the Dst index 1–6 hours in advance. Another method that combines ANNs and physical models was introduced by Bala and Reiff<sup>12</sup>. This combination method makes use of variables such as the solar wind speed, the interplanetary magnetic field (IMF) total strength, and the IMF's orientation. Lazzus et al.<sup>13</sup> optimized the connection weights within an ANN using a particle swarm optimization technique to improve the accuracy of Dst predictions. While the aforementioned techniques primarily focus on single-point predictions, Chandorkar et al.<sup>14</sup> proposed an extension by incorporating probabilistic forecasting into the Dst index. Their method builds autoregressive models using Gaussian processes (GPs). These models use the  $B_z$  component of the IMF, solar wind velocity, and historical Dst values to estimate the Dst index one hour ahead of time. This method produces a probability distribution of possible results instead of a single forecast. Moreover, these projections' average values might not be as precise as those generated by ANNs. To overcome this constraint, Gruet et al.<sup>9</sup> created a Dst prediction model that enhances the point prediction performance of GP by fusing GP with an LSTM network. By combining ANNs, support vector regression, and LSTM networks in a bagging framework, Xu et al.<sup>15</sup> routinely achieved a correlation coefficient ( $R$ )  $> 0.86$  and a root mean squared error (RMSE)  $< 8.09$  nT. Nuraeni et al.<sup>16</sup> studied a technique for Dst index forecasting 24 hours in advance. Using a nonlinear autoregressive exogenous (NARX) model trained on data from 39 geomagnetic storms between 1997 and 2000, they employed this methodology. Between August 1st and October 31st, 2021, the model was examined for operational Dst index prediction. The RMSE ranged approximately 5–20 nT on quiet days and 18–45 nT on disturbed days. For real-time Dst index forecasting, Nilam and Ram<sup>17</sup> presented a novel ensemble Kalman filter (EnKF) approach that makes use of ring current dynamics, such as injection and decay rates. The real-time Dst values or measurements of the horizontal magnetic field from a single ground-based magnetometer were added to this forecast to improve it. The outcomes show that the EnKF approach produced an RMSE of 4.3 nT and  $R = 0.99$ . To create operationally useful Dst projections, NASA's CoECI, the University of Colorado's CIRES, and NOAA's NCEI hosted the "MagNet: Model the Geomagnetic Field"<sup>18</sup> challenge in 2021. Managed by DrivenData and HeroX, the challenge attracted submissions of 1,197 models that used various CML strategies, which were validated using solar wind and Dst data in a containerized computing environment that simulated real conditions. Nair et al.<sup>19</sup> conducted additional analysis on the top four models, which were developed by Ali, Trotta, Medina and Medina, and Eissa and Amer<sup>18</sup>, based on their lowest RMSE errors. The ensemble averages of these models outperformed those of the individual models despite their different architectures.

Despite significant advancements, predicting the Dst index is still difficult because of the unpredictability of solar wind conditions and the constraints of current models. Over time, physics- and empirical-based models have been created to forecast Dst from solar wind data. However, they frequently have trouble making precise real-time forecasts, particularly during the peaks of geomagnetic storms and quiet times<sup>10,20–23</sup>. Conventional prediction models, mostly grounded in classical machine learning (CML) approaches, have been widely employed for geomagnetic storm forecasting. However, these models face severe limitations when attempting to handle the enormous dimensionality and inherent complexity of the datasets in question. Although intricate patterns and connections in the data are difficult for classical models to capture, they are essential for producing reliable predictions. This limitation leads to suboptimal performance and challenges in scaling these models effectively. One of the critical drawbacks of CML models, such as deep neural networks (DNNs), is their requirement for tuning millions of hyperparameters. This process is computationally intensive and demands substantial computing power. In addition, the amount of data required to train these models continues to increase, which increases the computing load in the post-Moore's Law age, when semiconductor technology developments have slowed. The progress and effectiveness of classical models in processing large-scale, real-time data streams utilized in geomagnetic storm prediction are severely hampered by this bottleneck. On the other hand, issues such as factoring large numbers and performing unstructured database searches are among the difficult challenges that quantum computing (QC) offers potential answers for<sup>24</sup>.

Quantum machine learning (QML)<sup>25–30</sup>, which leverages the principles of QC<sup>31–34</sup>, has shown superior performance in various domains compared to its classical counterparts<sup>35</sup>. One of the primary advantages of QML is its use of variational quantum circuits, which require significantly fewer model parameters than classical models<sup>36</sup>. This reduction in parameters helps mitigate the overfitting issues commonly associated with CML models. Moreover, variational quantum models can learn more efficiently and achieve higher test accuracy under certain conditions<sup>37</sup>. These methods excel in capturing complex patterns and dependencies in data, which are essential for accurate Dst predictions. Killoran et al.<sup>38</sup> developed quantum versions of specialized models such as residual, recurrent, and convolutional networks and showed how to integrate them into quantum formalism. Integrating quantum elements into a QML architecture, in which a classical computer updates the circuit parameters, improves the model's overall robustness and predictive power<sup>30,39</sup>. Larocca et al.<sup>40</sup> investigated the phenomena of over-parametrization in quantum neural networks (QNNs), characterizing it as a condition where a QNN has more parameters than a critical number, enabling it to explore all pertinent paths in state space. Efficient characterization of quantum states is essential to quantum computing, but conventional approaches become computationally costly. Certain quantum states may be identified using QNNs, which integrate feedforward, measurements, and unitary operations. Herrmann et al. utilized a 7-qubit superconducting quantum processor to find the topological phases of a spin model protected by symmetry<sup>41</sup>. Direct measurements of the string order parameter were not as good as the quantum convolutional neural network. For universal quantum computation, Beer et al.<sup>42</sup> suggested integrating a natural quantum perceptron into a QNN. Positive layer transition maps are utilized by the QNN design to provide a quantum analog of classical backpropagation. For noisy intermediate-scale quantum (NISQ) devices, the conventional simulation results of the QNN are encouraging. Wan et al.<sup>26</sup> proposed reversible and unitary quantum generalizations of classical neural networks. Gradient descent enables the QNN to carry out quantum generalizations of classical tasks efficiently. It can be applied photonically, compress quantum states, and find quantum communication protocols. Using QML, it is possible to overcome some of the fundamental issues raised by NISQ devices by creating noise-resistant quantum algorithms with controllable circuit depths<sup>43</sup>. This hybrid classical–quantum approach improves the performance and accuracy of Dst forecasting models and ensures that they are scalable and operationally feasible in real-time environments.

The motivation behind this research is driven by the urgent need to enhance the accuracy and reliability of Dst forecasting models, which are crucial for mitigating the impacts of geomagnetic storms on modern technological systems. Vital systems like GPS, satellite communication, and electric power transmission are interfered with by geomagnetic storms, which are generated by an efficient transfer of energy from the solar wind to the Earth's magnetic field. By enabling scientists and engineers to more accurately forecast the timing and severity of geomagnetic storm occurrences, improving these models contributes to protecting critical assets. This makes it possible to take preventative action to reduce damage and downtime.

Despite advancements in empirical, physics-based, and machine learning (ML) models over the past three decades, significant limitations persist. First, many existing models rely heavily on prior Dst values as input, but these values are often unavailable in real-time or contaminated with noise and baseline shifts, undermining their operational reliability. Second, real-time solar wind data, such as those from the NASA OMNI and RTSW data streams, frequently contain noise, gaps, and unprocessed information, complicating the accurate prediction of Dst. Finally, models must operate efficiently within the constraints of real-time computational environments, limiting the complexity and resource usage of potential forecasting solutions. Addressing these challenges is critical for improving the predictive performance and operational feasibility of Dst forecasting models, making them more robust and reliable for real-time use.

Researchers have been creating empirical models to predict Dst based on solar wind observations since the mid-1970s. These initiatives have relied heavily on satellite data such as NASA's Advanced Composition Explorer (ACE) and NOAA's Deep Space Climate Observatory (DSCOVR). However, forecasting extreme geomagnetic occurrences continues to be extremely difficult. Robust methods that can operate with unprocessed, real-time data streams under practical circumstances, such as noise and malfunctioning sensors, are needed.

By addressing these key areas, TriQXNet represents a significant advancement in Dst index forecasting, offering a robust, reliable, and interpretable solution for real-time applications. The model's nomenclature, TriQXNet, reflects its hybrid nature and the innovative approach it embodies. The "Tri" signifies the three parallel channels used in the architecture, each designed to handle different aspects of the data preprocessing and forecasting process. "Q" highlights the integration of QC with classical methods, an approach that is cutting-edge in the realm of geomagnetic storm forecasting. The "X" in TriQXNet stands for explainable AI (XAI) and uncertainty quantification (UQ), which are integral to our model's design. The inclusion of "Net" denotes the neural network foundation that underpins the model's predictive capabilities.

This research represents the pioneering application of interpretable and uncertainty quantifiable QC in space weather forecasting, a significant leap forward in leveraging QC for astronomical phenomena. The contributions of this research are as follows:

1. We introduce an innovative theoretical framework for forecasting geomagnetic storms using classical and QC techniques. This is the pioneering approach to combine conformal prediction and XAI with hybrid classical–quantum neural networks,

setting a new standard in space weather prediction.

2. A sophisticated data preprocessing pipeline has been developed, incorporating feature selection, normalization, aggregation of hourly features, imputation using the forward-fill method, and the most frequent strategy for dealing with noisy solar wind data from satellites.
3. We propose a hybrid classical–quantum neural network-based architecture with three parallel channels. Each channel processes preprocessed solar wind data to forecast the Dst index, enhancing robustness and accuracy. It is ready for operational deployment and can handle real-time data streams with inherent noise and gaps.
4. The model is designed to forecast the Dst index for both the current hour ( $t_0$ ) and the subsequent hour ( $t_{+1}$ ), providing valuable lead time for mitigating the effects of geomagnetic storms.
5. The model's improved accuracy is demonstrated by carefully evaluating its performance using RMSE and comparing it with that of 13 state-of-the-art hybrid models.
6. Through 10-fold cross-validated paired t-tests, we establish the statistical significance of TriQXNet's performance improvements.
7. By implementing conformal prediction techniques, we quantify the uncertainty in TriQXNet forecasts, providing confidence intervals that are crucial for operational decision-making.
8. By incorporating XAI concepts such as ShapTime and permutation feature importance, we enhance the interpretability of the model, making it easier to understand and trust its predictions.

The remainder of this article is organized as follows: In the "[Methods](#)" section, the architecture of all the developed models for benchmarking—which includes both classical and quantum components—is presented, along with information on the dataset description, experimental setup, and data preprocessing. The "[Results](#)" section covers the evaluation metric, our experimental findings, a comparison of TriQXNet's performance against the most advanced models, statistical validation, conformal prediction analysis, and XAI interpretation of TriQXNet. The probable advantages, practical ramifications, and real-world astronomical applications of the proposed method are discussed in the "[Discussion](#)" section. The paper's conclusions are detailed in the "[Conclusions](#)" section, offering a synopsis of the results and suggestions for future research.

## Methods

### Dataset description

The solar wind measurements collected from NASA's ACE and NOAA's DSCOVR satellites constitute the input data for this research, as shown in Fig. 1. The datasets included solar wind data, sunspot numbers, satellite coordinate data, and hourly Dst values. Table 1 provides detailed information on the solar wind dataset, satellite positions, and monthly smoothed sunspot numbers (Jan 1998 - Dec 2021), sourced from the SWPC, used in our research. Overall, 11,943,360 records are included in our dataset. Table 3 illustrates the six time periods for which we used Dst index data. The dataset's maximum and minimum Dst values are 77 nT and -422 nT, respectively.

### Solar wind data

We used solar wind data from NOAA's DSCOVR satellite (launched in 2015) and NASA's ACE satellite (in service since 1997) for our modeling work. The Lagrangian (L1) point is where both spacecraft are located, approximately 1.6 million kilometers from Earth. The fact that solar wind particles arrive at L1 approximately one hour before they strike Earth makes this position ideal for tracking solar activity. We used the 1-minute averaged data from 1998 to 2020 from NOAA's Space Weather Prediction Center (SWPC) in the "Real-Time Solar Wind" (RTSW) dataset. This collection contains important observations that were taken in almost real-time from the L1 site, including the IMF, density, temperature, and solar wind speed. The RTSW is not time-shifted to consider the transit time to Earth's magnetosphere, in contrast to other datasets. SWPC uses ACE data, which indicates when there are data outages or problems with DSCOVR.

### Spacecraft position data

The ACE and DSCOVR satellites circle around the L1 point, keeping their relative positions to Earth constant. The positions of these satellites, which are stored in geocentric solar ecliptic (GSE) coordinates, can improve the prediction accuracy of the Dst index.

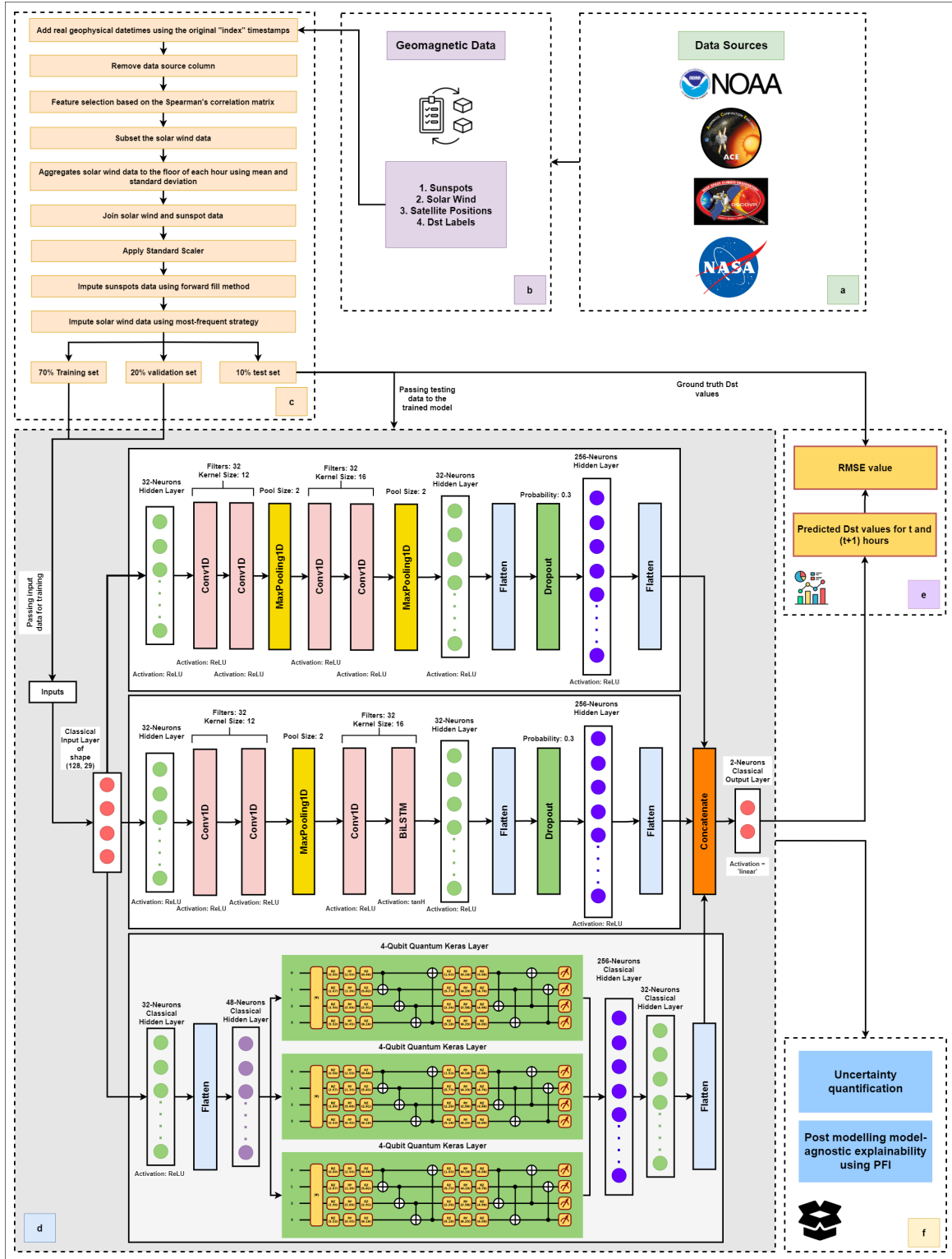


**Figure 1.** The methodological framework for Dst index forecasting using the TriQXNet architecture begins with (a) identifying and (b) collecting geomagnetic data from NASA's ACE and NOAA's DSCOVR satellites. (c) The data undergo robust preprocessing techniques to ensure quality and compatibility with the model. (d) The framework's core is the proposed hybrid classical-quantum TriQXNet architecture. (e) TriQXNet forecasts the Dst index for  $t_0$  and  $t_{+1}$  hours and is evaluated based on the RMSE. (f) Finally, the framework proposes the implementation of UQ and XAI techniques.



**Table 1.** Features of solar wind input data, spacecraft positional data, and sunspot numbers along with their respective units

Feature Name	Description	Unit
time_delta	Time interval since the start of a segment	–
bx_gse	X-component of the IMF in geocentric solar ecliptic (GSE) coordinates	nT
by_gse	Y-component of the IMF in GSE coordinates	nT
bz_gse	Z-component of the IMF in GSE coordinates	nT
bx_gsm	The IMF's X-component in geocentric solar magnetospheric (GSM) coordinates	nT
by_gsm	The IMF's Y-component in GSM coordinates	nT
bz_gsm	The IMF's Z-component in GSM coordinates	nT
theta_gse	The angle between the magnetic vector B and the ecliptic plane, which is positive when B points north, is the latitude of the IMF in GSE coordinates	degrees
phi_gse	The angle between the Earth-Sun direction and the IMF vector projection on the ecliptic plane is known as the IMF's longitude in GSE coordinates	degrees
theta_gsm	Latitude of the IMF in GSM coordinates	degrees
phi_gsm	Longitude of the IMF in GSM coordinates	degrees
bt	Magnitude of the IMF component	nT
Density	Proton density in the solar wind	$N/cm^3$
Speed	Bulk speed of the solar wind	km/s
Temperature	Ion temperature of the solar wind	Kelvin
Magnetic and Plasma Source	From 2016 onwards, solar wind data quality determines if it comes from DSCOVR or ACE satellites, indicated by "ds" for DSCOVR and "ac" for ACE	–
GSE_X (km)	Satellite location relative to GSE coordinates in the X direction	Kilometers
GSE_Y (km)	Satellite location relative to GSE coordinates in the Y direction	Kilometers
GSE_Z (km)	Satellite location relative to GSE coordinates in the Z direction	Kilometers
smoothed_ssn	Sunspot numbers for each month averaged over time	Numbers

### Sunspot numbers

Sunspot numbers, which follow an approximately 11-year solar cycle, influence geomagnetic activity. Our dataset spans solar cycles 23 and 24, covering periods when geomagnetic storms are most frequent. Using sunspot data helps calibrate our model to predict geomagnetic activity throughout different solar cycle phases.

### Dst data

The World Data Center for Geomagnetism in Kyoto provides the Dst index, which is used to quantify the strength of geomagnetic storms<sup>3</sup>. We used hourly Dst data from 1998 to 2020, including final, provisional, and real-time values. The Dst index represents the average geomagnetic activity over each hour. When TriQXNet forecasts the Dst index, it uses solar wind data up to that hour to predict the average Dst for the following hour. This methodology ensures that our forecasts are forward-looking and accurate. Our focus is on predicting extreme geomagnetic events, defined as periods when the Dst index is  $-80$  nT or lower, due to their significant impact on technology and infrastructure (see Fig. 2). The dataset includes events with Dst values as low as  $-422$  nT, highlighting the severity of these disturbances. A crucial step in developing TriQXNet and ensuring its interpretability involves exploring feature correlations. As depicted in Fig. 3, there is a significant correlation between  $|Dst|$  and bulk speed of the solar wind (0.46), magnitude of the IMF component  $bt$  (0.31), ion temperature of the solar wind (0.25), and  $bz_{gsm}$  (0.20). Conversely, there is little correlation between  $|Dst|$  and the positions of the ACE and DSCOVR satellites. Understanding these correlations helps refine TriQXNet's architecture and sensitivity to various input parameters. Further details on model performance and XAI techniques are discussed in the "Results" section.

### Experimental setup

The hardware and software configurations used in our studies are shown in Table 2. The Python version, CPU, GPU, RAM, and important libraries used in our study are detailed.

### Data preprocessing

We begin our data preprocessing by exploring the input (feature) and output (label) data to understand their architecture, statistical properties, and basic input-output relationships. Given the vast amount of solar wind data (8,392,320 rows across 15 features), we performed a similar analysis for sunspots. These initial steps provided insights into each feature's range, central tendency, and variability, which is fundamental for effective preprocessing. One major challenge in working with real-time

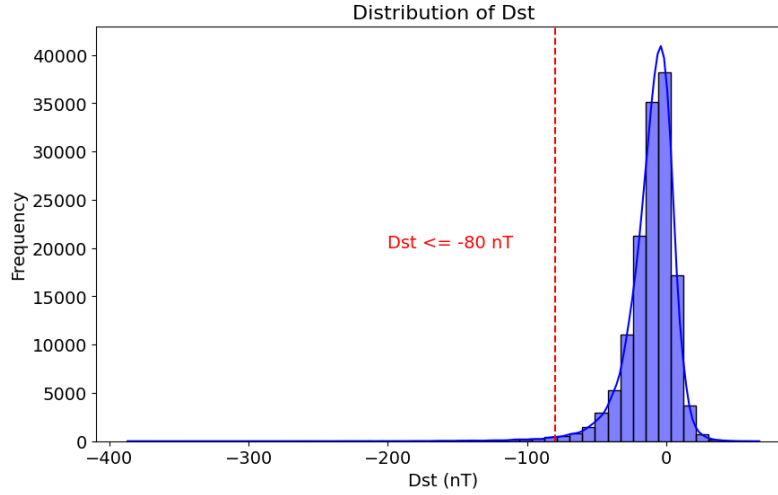


**Figure 2.** Distribution of Dst values within the dataset, with extreme events marked by the red line at -80 nT or below.

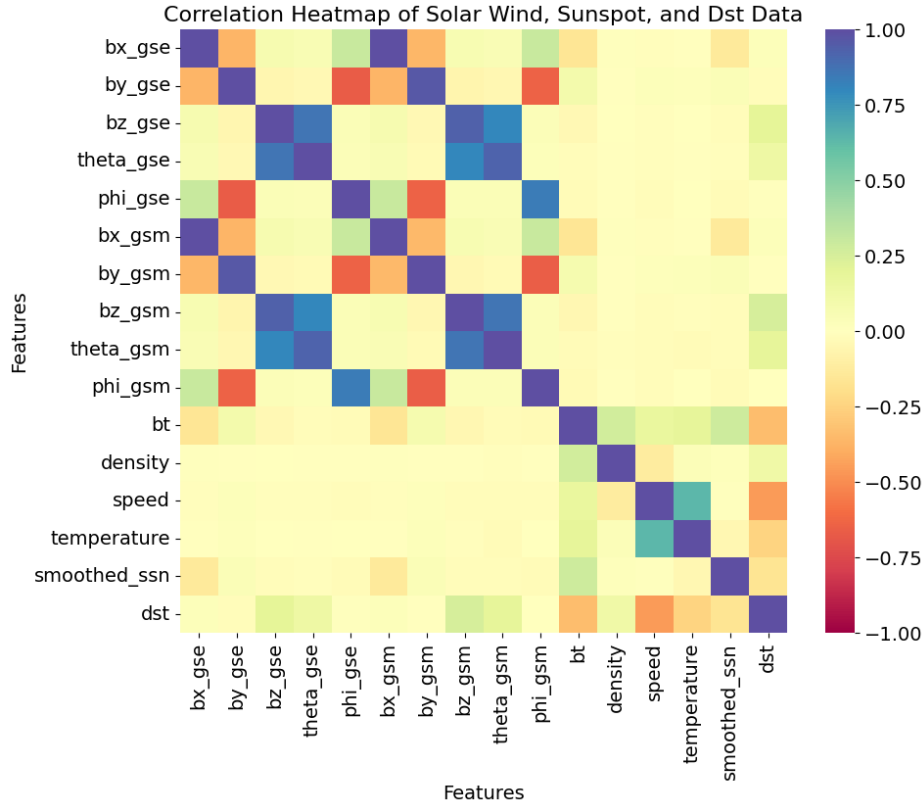


**Figure 3.** Heatmap showing the Dst index, different solar wind characteristics, and the Pearson connection matrix for different sunspot numbers. The spectrum from a perfect negative correlation to a perfect positive correlation is represented by the color gradient, which ranges from -1 to +1. The variables on the x and y-axes are the same; the solar parameters are represented by the first 15 columns and rows, and the Dst index is represented by the last column and row.

solar wind data is the presence of gaps. To address this, we calculated the percentage of missing data for each feature, finding gaps ranging from approximately 3.8% to 9.7%. This highlights the need for robust imputation techniques to maintain data integrity. We used imputation techniques such as forward-filling for sunspot data and the most frequent value imputation for solar wind observations to fill these gaps, ensuring that no missing values remained after postprocessing.

We generated features by aggregating the solar wind data to the floor of each hour, computing statistics such as the hourly

**Table 2.** Computational environment details

Resource	Specification
CPU	Intel(R) Xeon(R) with x86 architecture, 2 GHz clock speed, 4 virtual cores, 18 GB memory
GPU	Dual NVIDIA T4, each with 2560 CUDA cores and 16 GB memory
RAM	32 GB DDR4
Python version	3.10.12
Software libraries	numpy, pandas, matplotlib, plotly, scikit-learn, TensorFlow, Keras, os, urllib, zipfile, scipy, crepes, qiskit, PennyLane-qiskit, pylatexenc, PennyLane

**Table 3.** Time ranges of each period from which the data were collected

Period	From (YYYY/MM/DD) (HH:MM:SS)	To (YYYY/MM/DD) (HH:MM:SS)
1	1998/02/16 (00:00:00)	2001/05/31 (23:59:00)
2	2013/06/01 (00:00:00)	2019/05/31 (23:59:00)
3	2004/05/01 (00:00:00)	2010/12/31 (23:59:00)
4	2001/06/01 (00:00:00)	2004/04/30 (23:59:00)
5	2011/01/01 (00:00:00)	2013/05/31 (23:59:00)
6	2019/06/01 (00:00:00)	2020/10/31 (23:59:00)

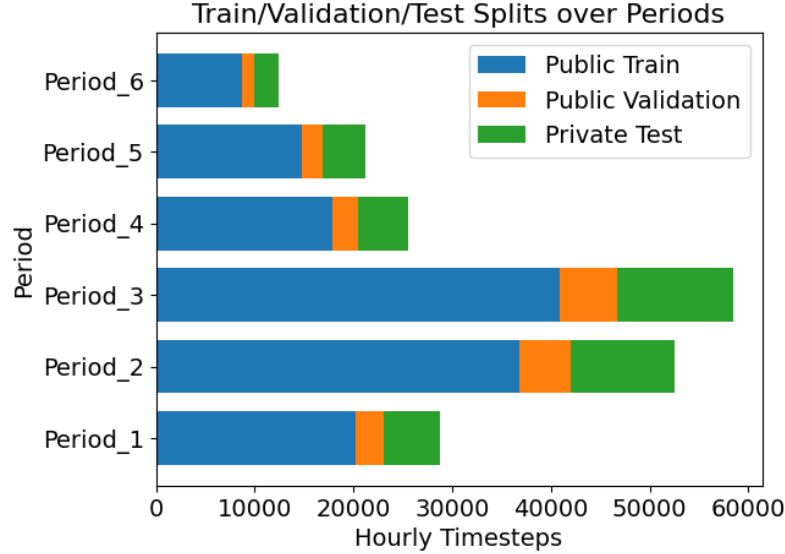


**Figure 4.** Distribution of training, validation, and test data across six periods. The x-axis represents the hourly timesteps, while the y-axis indicates the six periods labeled as Period 1 through Period 6. The lengths of the bars correspond to the number of hourly timesteps allocated to each data split. The blue bars represent the training data, the orange bars indicate the validation data, and the green bars show the test data.

mean and standard deviation. This aggregation step reduces noise and variability, making the data more suitable for modeling. The aggregated data are then combined with sunspot observations to enrich our feature set. Using the conventional scaling normalization procedure, which centers the data around zero with unit variance, we subtracted the mean and divided the result by the standard deviation. These steps are essential for ensuring that our model can effectively learn from the data without being biased by variations in scale or magnitude among the features. This step used ‘StandardScaler’ from the ‘sklearn’ library. Scaling maintains characteristics with wider ranges, from controlling the model training process to aiding in the acceleration of gradient-based optimization techniques convergence. To forecast the present ( $t_0$ ) and next hour ( $t_{+1}$ ) values, we constructed a time-shifted version of the Dst index for the output labels. This formulation aligns with our goal of forecasting immediate and near-future geomagnetic disturbances, which is critical for timely space weather alerts. Finally, we combined the processed features and labels into a single data frame. This merged dataset is then split into training, validation, and test sets, ensuring that all splits adequately represent each period (train\_a, train\_b, train\_c), as illustrated in Table 3.



To ensure that the model performs effectively when applied to new data, we split the dataset into three parts: 70% training, 20% validation, and 10% test sets. We first split the data into periods and calculated the length of each period. Based on the provided ratios, we determine how many samples are needed for the test and validation sets for each time. As shown in Fig. 4, the period data are then divided as follows: the last piece is assigned to the test set, the section that came before the validation set, and the remaining data to the training set. This methodical technique guarantees that every period is sufficiently represented in all subsets, maintaining the temporal structure and enabling a thorough assessment of the model's effectiveness. To prepare our modeling data, we transformed our training, test, and validation datasets into data point sequences, each comprising 128 timesteps. For each period in our data, we matched these sequences with the corresponding target values and grouped them into batches of 768, shuffling them to ensure that our model trained effectively.

## Model development for benchmarking

### LSTM

Since the long short-term memory (LSTM) network is a well-known recurrent neural network (RNN) that can successfully replicate sequential data<sup>44</sup>, we have selected it as our baseline model in this research. The architecture of our LSTM model, including a single layer with 512 neurons and a dropout rate of 0.4, is represented by equation (1).

$$h_t = \zeta (W_{hh}h_{t-1} + W_{xh}x_t + b_h) \quad (1)$$

The input and hidden state are represented by  $x_t$  and  $h_t$ , respectively, at time  $t$ . The activation function, which is usually a sigmoid or hyperbolic tangent, is represented by  $\zeta$ . The weight matrices for the input and hidden state are represented by  $W_{xh}$  and  $W_{hh}$ , and the bias term is  $b_h$ . We add a 2-neuron fully connected dense layer (equation (2)) after the LSTM layer to provide the final output predictions.

$$y = W_d h_t + b_d \quad (2)$$

The weight matrix of the dense layer is represented by  $W_d$ , the output from the LSTM layer is represented by  $h_t$ , the bias term is represented by  $b_d$ , and the output is denoted by  $y$ . Because we have configured the model to be stateless, it can handle input sequences on its own.

### HybridTransNet

To create a hybrid architecture, we combined Transformer encoders with convolutional neural networks (CNNs) inspired by the most advanced available time series classification methods. HybridTransNet highlights the hybrid nature of the model, incorporating both traditional RNN components (such as LSTM and GRU) and modern transformer-based elements. We concatenate a linearly spaced timestep feature after the input layer to enhance the temporal context, which is normalized between  $-0.5$  and  $0.5$ . The input and timestep features are then combined using a concatenation layer. A 1D convolutional layer with a total of 256 filters and a kernel size of 1 process this combined input. After the first convolution, the data are passed through a stack of six Transformer encoder blocks. With two heads for multihead self-attention, each Transformer encoder block contains a feed-forward network (FFN). The representation of the self-attention mechanism is as follows:

$$\text{Attention}(\mathbf{Q}, \mathbf{K}, \mathbf{V}) = \text{softmax} \left( \frac{\mathbf{Q}\mathbf{K}^T}{\sqrt{d_k}} \right) \mathbf{V} \quad (3)$$

the dimension of the key vectors is denoted by  $d_k$ , and the query, key, and value matrices are represented by  $\mathbf{Q}$ ,  $\mathbf{K}$ , and  $\mathbf{V}$ , respectively.

The self-attention layer's output is normalized and added to the input (residual connection). A two-layer feed-forward network comes next. The model uses multilayer perceptron (MLP) post-transformer layers, which are composed of dense layers with 128 and 64 neurons, each followed by a dropout layer to avoid overfitting. The output layer, which creates the final prediction, is composed of a thick layer containing two neurons.

### Stacked BiLSTM

This model enhances the prediction capability of our baseline LSTM model by utilizing a bidirectional long short-term memory (BiLSTM) architecture. The sequences are returned by the 256 neurons in the first BiLSTM layer, which has a 0.1 dropout rate. This is followed by three more BiLSTM layers, each with 125 neurons and a dropout rate of 0.1, with the first two layers returning sequences to ensure that the full depth of the model is utilized and the final BiLSTM layer not returning sequences to prepare for the dense output layers. Two neurons make up the output layer of the dense layers, while eight neurons make up the

hidden layer. The forward and backward passes of the BiLSTM may be represented mathematically by the equations (4) and (5).

$$\vec{h}_t = \text{LSTM}(x_t, \vec{h}_{t-1}) \quad (4)$$

$$\overleftarrow{h}_t = \text{LSTM}(x_t, \overleftarrow{h}_{t+1}) \quad (5)$$

Equation (6) illustrates how the forward and backward passes are concatenated to offer the whole context for each timestep.

$$h_t = [\vec{h}_t, \overleftarrow{h}_t] \quad (6)$$

The architecture is inspired by the work on BiLSTMs by Schuster and Paliwal and is known for its effectiveness in various sequence modeling tasks<sup>45,46</sup>.

### **BiLSTM+BiGRU**

The input layer of this model architecture receives input data first, after which it passes via a BiLSTM layer of 488 neurons and a BiGRU layer with 1464 neurons. Timesteps are processed successively by each layer, with the results of one phase feeding into the next. The "forget gates" in LSTM and GRU cells eliminate unnecessary old data while keeping what is essential. Long sequences can be handled with this method without the risk of error gradients being too big, which is a common problem with previous RNNs. Mathematically, the forward and backward passes of the GRU layers can be represented by equation (7).

$$h_t^{GRU} = \text{GRU}(x_t, h_{t-1}^{GRU}) \quad (7)$$

Both the LSTM and GRU layers are configured to return sequences. The outputs from the GRU layer are flattened and then passed through a series of dense layers with decreasing neuron counts (96, 128, and 64) to extract and consolidate the features learned from the sequential data. The model's mathematical expressiveness remains unchanged with the addition of these dense layers. Net linear functions can always be used in place of linear functions when they are composable. On the other hand, these modifications could affect the initial state or the convergence behavior. To generate the final predictions, a dense output layer consisting of two neurons is added at the end.

### **DeepSeqConvNet**

The ensemble of 21 convolutional neural network (CNN) models, each composed of four blocks, is known as the DepSeqConvNet architecture<sup>19</sup>. Within each block, two consecutive convolutional layers are connected. The forward pass through the convolutional layers can be mathematically represented by equation (8).

$$z_i^{(l)} = \text{Conv}(x_i^{(l-1)}) \quad \text{for } i = 1, 2, \dots, n \quad (8)$$

For the  $i^{th}$  input,  $x_i^{(l-1)}$  is the input to layer  $l$ , and  $z_i^{(l)}$  is the output of the convolutional layer  $l$  for the  $i^{th}$  input.

Following these convolutions, leaky rectified linear unit (ReLU) activation and subsequent max pooling operations are applied, reducing the sequence length by half. Additionally, the network incorporates a skip connection, concatenating the input's last timestep with the convolutional segment's output before reaching the final output layers. This model employs a custom loss function, characterized by its formulation in equation (9).

$$\text{Loss} = \log((y - s)^2)^s + |y - s| \quad (9)$$

Here, the power  $s$  controls the loss function's behavior, allowing for adjustments in both under and overestimation. This loss function approximates the RMSE by averaging the logarithm of the squared error. The parameter  $s$  plays a crucial role in fine-tuning the loss function's response to the RMSE. Specifically, when  $s = 2$ , the second component of the loss resembles the mean squared error. Stronger penalties are applied to outliers with higher  $s$  values, which indicate heightened sensitivity to severe mistakes. This phenomenon stems from formulating the loss function's second term, accentuating the impact of significant deviations. Large error minimization is prioritized by higher  $s$  values, which improve the model's performance on extreme data points. With seven random seeds for every variant and the designated loss function with  $s$  values of 1.5, 2.4, and 2.5, the DeepSeqConvNet ensemble consists of 21 trained models.

### ***TemporalFusionCNN Ensemble***

TemporalFusionCNN is a robust CNN architecture with several sequential convolutional layers that detect increasing patterns over different time frames. After data processing, each convolutional layer output's last data point is concatenated and routed through a thick layer. Information spanning several periods in history prior to the forecast time is gathered using the last data point in a convolution. For example, information from the past hour may be included in the final feature in the first layer, and information from the preceding six hours may be included in the features in the next layer.

The design of TemporalFusionCNN is similar to that of the U-Net, consisting of a "contracting path" with a few convolutional layers that compress the picture and a "expansive path" with upconvolution layers that restore the image to its initial size.<sup>47</sup> Local predictions consider global aspects. In contrast, the temporal convolutional network uses residual connections, where low- and high-level features are combined by addition rather than concatenation<sup>48</sup>.

The TemporalFusionCNN ensemble consists of five identical models trained on different data parts. Two predictions,  $t$  and  $t + 1$ , are made with separate models, resulting in 10 models. Here, ensemble averaging is used because it might be problematic for individual models to accurately represent the true connection between input and output variables, frequently resulting in fitting noise in the training set. Averaging the predictions of multiple models cancels out random noise, providing a smoother and more accurate estimate of the underlying relationship.

### ***CNN+BiLSTM+Multihead Attention***

We developed a multi-pathway neural network called CNN+BiLSTM+Multihead Attention, which consists of three main pathways: an LSTM network, a CNN, and a multi-head attention mechanism.

Input, convolutional, and batch normalization layers are the first layers in the CNN pathway. More precisely, batch normalization happens after the first convolutional layer—a kernel size of three—which consists of sixteen filters. After the ReLU activation and batch normalization, three convolutional layers with 32 filters, a kernel size of 4, and 'same' padding are used. Max-pooling processes are interspersed to downsample the feature maps without losing important features. The flattened features are then put into a thick layer of sixty neurons.

Concurrently, BiLSTM layers with 512, 256, and 128 units are used by the LSTM route to process the input sequence. The outputs of these LSTM layers are concatenated and then routed through thicker layers. A second dense layer with a single neuron is used to generate the final output after the first layer with 128 units and a SELU activation function. The output is then flattened for integration with the remainder of the model architecture.

To capture self-attention inside the input sequence, a multihead attention layer with three heads and a head size of three is used. A 1D vector is created by flattening the output of the multihead attention layer.

The CNN, LSTM, and multihead attention pathways' combined outputs are concatenated in the model's output layer, which is a dense layer composed of two neurons.

### ***CNN+BiLSTM+Multihead Attention+TimeDistributedDense***

The CNN+BiLSTM+Multihead Attention model and this model's architecture are quite similar, except that this model has additional Time-Distributed layers and different parameters. Following a TimeDistributed layer, a dense layer of 32 neurons and a ReLU activation function is distributed using the input data.

We use the output of the layer before it to start a convolutional operation for the convolutional layers. To be more precise, a Conv1D layer is set up with 32 filters, a 12 kernel size, and a 1 stride. Afterward, batch normalization accelerates convergence and stabilizes the learning process. The next step involves applying three convolutional blocks iteratively. Two convolutional layers with 32 filters, 12 and 16 kernel sizes, and the same padding to maintain spatial dimensions make up each block. Following each convolutional layer was the inclusion of ReLU activation and batch normalization. To improve the gradient flow and lessen the vanishing gradient issue, a skip connection is also created between the first feature representation and the output of the second convolutional layer. By using max pooling with a pooling size of three, the feature maps are downsampled. Ultimately, the output was prepared for additional processing by applying a TimeDistributed dense layer with 60 neurons and ReLU activation.

In the second input model, temporal relationships are bidirectionally captured by a BiLSTM layer consisting of 512 units. The output of this layer is concatenated with the original input sequence along the feature axis. The first BiLSTM layer's output and the second BiLSTM layer's output—which has 256 units applied—are concatenated. To improve temporal understanding of the input sequence, this process is repeated in the third BiLSTM layer (128 units). The outputs from each BiLSTM layer are concatenated along the feature axis.

Attention mechanisms are added to the model using a multihead attention layer with three heads and a head size of three. This layer allows the model to focus on various input stream segments simultaneously. A 1D vector is created by flattening the output of the multihead attention layer. A 0.3 dropout rate is used to regularize the attention layer's output.

The outputs from the CNN, LSTM, and multihead attention pathways are joined together, followed by a dense layer with 256 neurons and ReLU activation to improve the feature representation. The model architecture is completed by a dense output

layer that has two neurons, making it ready for task-specific training and assessment.

### ***CNNDenseNet***

The architecture of CNNDenseNet is characterized by a sequence of convolutional layers designed to capture patterns over progressively longer periods within the input data. It begins with an initial convolution layer followed by batch normalization. Subsequently, the output of this layer undergoes a series of five convolutional blocks. Each block consists of a convolutional layer comprising 32 filters and a kernel size of 6. Batch normalization is then applied to further stabilize training. Nonlinearity is introduced by a ReLU activation function. After batch normalization, another convolutional layer with 16 filters and a kernel size of 3 was used. Concatenation preserves features learned at previous levels by combining each block's output with the first layer's output. Before the max-pooling step, we apply a final ReLU activation function with a pooling size of 3 and stride of 2.

After the convolutional and pooling layers, the output is flattened into a 1D vector, and then it passes through two dense layers. A ReLU activation function is incorporated into the first dense layer, which consists of 64 units. A second dense layer, consisting of 32 units, is then added. When training, a dropout layer is applied with a 0.3 dropout rate, randomly zeroing out certain input units. The dense layer is responsible for generating the final predictions at the end of the network.

### ***CNNEncoderDecoder***

The encoder and decoder components of the CNNEncoderDecoder architecture are arranged in an autoencoder-like manner. After the input layer, a time-distributed dense layer with 32 ReLU activation neurons is added. We add three convolutional layers with 64, 32, and 16 filters and 12, 12, and 16 kernel sizes, respectively, to the encoder component. After every convolutional layer, there are two max-pooling operations. To provide nonlinearity, we apply the ReLU activation function over the encoder.

Moving on to the decoder, we utilize matching convolutional layers to extract the input data from the encoded representation. The decoder mirrors the structure of the encoder with convolutional layers and upsampling operations. The decoder layers consist of convolutional layers with 16, 32, and 64 filters and 12, 12, and 16 kernel sizes, respectively, with ReLU activation followed by upsampling operations.

After the decoder, a 1D convolutional layer with a single filter and a kernel size of 16 is added to process features using the scaled exponential linear unit (SELU) activation function. Next, a 128-neuron time-distributed dense layer with ReLU activation is deployed. The output is reshaped for further processing by a flattening layer. The features are then enhanced by a dense layer consisting of 256 neurons and ReLU activation, while regularization is applied using a dropout layer with a 0.3 rate. The dense output layer of the model consists of two neurons.

### ***Multichannel CNN+BiLSTM***

In the architecture design, the multichannel CNN+BiLSTM begins with an input layer followed by the convolutional layers. The first step of the convolutional operation involves 16 filters with a kernel size of 3 and strides of 1. Batch normalization is applied to stabilize the training process, ensuring efficient convergence. Next, five convolutional blocks are employed, each comprising convolutional layers with 32 filters and kernel sizes of 4 and 2, respectively, with ReLU activation. Moreover, each convolutional layer is combined with batch normalization. The output of the first layer is combined with the output of each convolutional block through a concatenation operation. Max-pooling reduces dimensionality by using two strides and a pooling size of three. A time-distributed dense layer with 60 neurons and ReLU activation is applied, and the layer is then flattened.

Two-way temporal dependencies are recorded by a BiLSTM layer (768 units) in the second input model. The first two 512-unit BiLSTM layers are then applied; the first one processes the original input sequence, while the second one processes the output of the BiLSTM layer that came before it. Along the feature axis, the outputs of these layers are concatenated. Then, two sets of BiLSTM layers are used, with 384 and 256 units and 384 and 128 units, respectively, in each set. In a manner identical to the preceding step, these layers are concatenated. The outputs of the BiLSTM layers, which include the combined temporal representations from every layer, are concatenated along the feature axis. Next, a 128-unit dense layer with an activation function of SELU is employed. To prevent overfitting, dropout regularization at a rate of 0.2 is applied after the LSTM layer. The last thick layer is applied with a single neuron to produce the final, flattened output.

In the third input model, an inception module captures multiscale features from the input data. This module comprises several convolutional operations with different filter sizes and bottleneck layers to efficiently capture features at various scales. The inception module is applied iteratively for a total of 6 times, with the option to include residual connections every third iteration for improved feature propagation. A global average pooling layer is applied to the output of the inception module to obtain a compact feature representation. Subsequently, a dense layer with 2 neurons produces the output for the third input model.

The outputs of the LSTM, inception, and convolutional pathways are combined. On the combined features, 0.2-rate dropout regularization is then applied. The final output is produced by processing the combined features through two additional dense layers: one with 128 units and a SELU activation function and the other with 2 neurons.

### **CNN+BiLSTM+TimeDistributedDense**

After CNN+BiLSTM+TimeDistributedDense defines an input layer, the model architecture of the A TimeDistributed layer is used to distribute a dense layer with 32 neurons and ReLU activation throughout each timestep of the input sequence. The next step involves using two convolutional layers, each with 32 filters and 12 kernel sizes. To preserve spatial dimensions, ‘same’ padding and ReLU activation functions are employed. A max-pooling layer with a pooling size of two is then added after that. Subsequently, a 32-unit BiLSTM layer records bidirectional temporal dependencies and output sequences. A second time-distributed dense layer is deployed with ReLU activation and 32 neurons. Next, a 1D vector is created by flattening the output. A 0.3 dropout regularization rate is utilized. Two dense layers—the final output layer, which has two neurons and generates the model’s predictions—come next. The first has 256 neurons and ReLU activation.

### **Conv1DTimeDistributedNet**

Conv1DTimeDistributedNet begins with an input layer and applies a TimeDistributed layer afterward, distributing a dense layer with 32 neurons and ReLU activation over each timestep of the input sequence. When it comes to extracting spatial characteristics from the input sequence, the convolutional layers take over after the TimeDistributed layer. The first two convolutional layers have 32 filters and a kernel size of 12 each. ReLU is used to activate them. Following these layers are the max-pooling operations with a pooling size of two. ReLU activation and max-pooling are carried out after applying two additional convolutional layers, each with 32 filters and a 16-bit kernel size. After the convolutional layers, a second TimeDistributed layer with a dense layer of 32 neurons and ReLU activation is used. The output is then flattened to produce a 1D vector. A dropout regularization with a rate of 0.3 is applied before the flattened features are passed through a dense layer with 256 neurons and ReLU activation. A layer with two neurons makes up the output layer, which generates the final predictions.

### **Proposed TriQXNet**

The proposed TriQXNet hybrid classical–quantum parallel model architecture consists of a single QNN with three concatenated 4-qubit quantum circuits and two hybrid classical deep neural networks, as illustrated in Fig. 1 and Table 4. The hybrid classical models are analogous to the modified versions of Conv1DTimeDistributedNet and CNN+BiLSTM+TimeDistributedDense. TriQXNet was constructed using TensorFlow 2.14.0, NumPy 1.23.5, SciPy 1.13.0, and the PennyLane library (version 0.34.0), all implemented in Python. This architecture aims to extract temporal and spatial features from the input data while incorporating quantum computational advantages. The input layer accommodates sequences of 128 timesteps, each with a feature dimension equal to 29, as shown in Table 4. The data parallelly pass through three distinct processing pipelines to capture different input aspects.

#### **Pipeline 1: Classical modified Conv1DTimeDistributedNet**

In the first pipeline of TriQXNet, a series of classical neural network layers are employed to process the input solar wind data, which resembles the modified Conv1DTimeDistributedNet model. This pipeline begins with a TimeDistributed dense layer, which independently applies a dense transformation with 32 neurons and ReLU activation across each timestep. This operation can be mathematically expressed as:

$$h_t = \text{ReLU}(W \cdot x_t + b) \quad (10)$$

where  $\text{ReLU}(z) = \max(0, z)$ ,  $W$  and  $b$  are the weights and biases, respectively, and  $x_t$  denotes the input at timestep  $t$ . Convolutional layers are then applied one after the other. In order to preserve the input dimensions, the first set of Conv1D layers—each with 32 filters and a kernel size of 12—performs convolution operations using ReLU activation and ‘same’ padding. This operation is given by:

$$h_t = \text{ReLU} \left( \sum_{k=0}^{K-1} W_k \cdot x_{t+k} + b \right) \quad (11)$$

where the bias is represented by  $b$ , the convolutional weights are represented by  $W_k$ , and the kernel size is represented by  $K$ . A MaxPooling1D layer with a pool size of 2 follows these layers. It lowers the dimensionality by utilizing the maximum value within each window of two timesteps:

$$h_t = \max(x_{2t}, x_{2t+1}) \quad (12)$$

The next convolutional block includes two Conv1D layers with 32 filters and a kernel size of 16, as well as ReLU activation and ‘same’ padding. These layers further extract features over longer periods, represented as:

$$h_t = \text{ReLU} \left( \sum_{k=0}^{K-1} W_k \cdot x_{t+k} + b \right) \quad (13)$$



**Table 4.** Pipeline components and parameters for TriQXNet

Pipeline	Component	Parameters
1: Classical modified Conv1DTimeDistributedNet	Input Layer	Shape: (128, 29)
	TimeDistributed Dense	Units: 32, Activation: ReLU
	Conv1D Layer 1	Filters: 32, Kernel Size: 12, Activation: ReLU, Padding: same
	Conv1D Layer 2	Filters: 32, Kernel Size: 12, Activation: ReLU, Padding: same
	MaxPooling1D Layer	Pool Size: 2
	TimeDistributed Dense	Units: 32, Activation: ReLU
	Dropout	Rate: 0.3
	Dense Layer	Units: 256, Activation: ReLU
	Flatten Layer	-
2: Classical modified CNN+BiLSTM+TimeDistributedDense	Input Layer	Shape: (128, 29)
	TimeDistributed Dense	Units: 32, Activation: ReLU
	Conv1D Layer 1	Filters: 32, Kernel Size: 12, Activation: ReLU, Padding: same
	Conv1D Layer 2	Filters: 32, Kernel Size: 12, Activation: ReLU, Padding: same
	MaxPooling1D Layer	Pool Size: 2
	Conv1D Layer 3	Filters: 32, Kernel Size: 16, Activation: ReLU, Padding: same
	Bidirectional LSTM	Units: 32, Return Sequences: True
	TimeDistributed Dense	Units: 32, Activation: ReLU
	Dropout	Rate: 0.3
	Dense Layer	Units: 256, Activation: ReLU
	Flatten Layer	-
3: Dressed quantum circuit	Input Layer	Shape: (128, 29)
	TimeDistributed Dense	Units: 32, Activation: ReLU
	Flatten Layer	-
	Dense Layer for Qubits	Units: $2^{n_{qubits}} * 3$ (for amplitude embedding, where $n_{qubits} = 4$ )
	Split into 3 parts	Each part: $48 \div 3 = 16$ features
	Quantum Layer 1	Input: 16 features, Qubits: 4, Output: $\log_2^{16} = 4$ features
	Quantum Layer 2	Input: 16 features, Qubits: 4, Output: $\log_2^{16} = 4$ features
	Quantum Layer 3	Input: 16 features, Qubits: 4, Output: $\log_2^{16} = 4$ features
	Concatenate Quantum Outputs	$4 \times 3 = 12$ features
	Dense Layer	Units: 256, Activation: ReLU
	Flatten Layer	-

with  $K$  now being 16. Another MaxPooling1D layer follows to condense the feature maps further:

$$h_t = \max(x_{2t}, x_{2t+1}) \quad (14)$$

A second TimeDistributed dense layer with 32 neurons and ReLU activation is implemented to preserve the temporal structure and increase nonlinearity:

$$h_t = \text{ReLU}(W \cdot x_t + b) \quad (15)$$

A dropout layer with a rate of 0.3 is added to reduce overfitting. During each update cycle, 30% of the neurons are randomly set to zero. The dropout function has the following expression:

$$h_t = \begin{cases} 0 & \text{with probability 0.3} \\ \frac{h_t}{0.7} & \text{with probability 0.7} \end{cases} \quad (16)$$

The pipeline concludes with a dense layer comprising 256 neurons and ReLU activation, aggregating the learned features into a comprehensive representation:

$$h = \text{ReLU}(W \cdot x + b) \quad (17)$$

Finally, the features are flattened into a one-dimensional vector, which is used for integration with other parallel pipelines or for final output prediction.

#### **Pipeline 2: Classical modified CNN+BiLSTM+TimeDistributedDense**

The second pipeline in TriQXNet integrates classical convolutional and LSTM layers to process solar wind data, leveraging both spatial and temporal features, which resembles the modified CNN+BiLSTM+TimeDistributedDense model. A TimeDistributed dense layer comprising 32 neurons and ReLU activation applied to each timestep of the input sequence independently forms the first part of the pipeline. The next two Conv1D layers have the same padding to maintain the input length, a kernel size of 12, 32 filters, and ReLU activation. The extraction of local features from the input sequence is improved by these layers. The temporal dimension is then reduced by a MaxPooling1D layer with a pool size of 2 by calculating the maximum value within



each window of two timesteps. This is followed by another Conv1D layer with 32 filters and a kernel size of 16, applying ReLU activation and ‘same’ padding. A BiLSTM layer with 32 units is then employed, capturing long-term dependencies in the data from both forward and backward directions. The BiLSTM can be mathematically described as:

$$\vec{h}_t = \text{LSTM}(x_t, \vec{h}_{t-1}, \eta) \quad (18)$$

$$\overleftarrow{h}_t = \text{LSTM}(x_t, \overleftarrow{h}_{t+1}, \eta) \quad (19)$$

$$h_t = \text{Concat}(\vec{h}_t, \overleftarrow{h}_t) \quad (20)$$

where the hidden states of the forward and backward LSTMs are denoted by  $\eta$  and  $\vec{h}_t$  respectively, and  $\eta$  stands for the LSTM parameters. Next, 32 neurons and ReLU activation are added to another TimeDistributed dense layer. To avoid overfitting, there is a dropout layer with a rate of 0.3. This causes 30% of the neurons to be randomly set to zero during training. Following is a dense layer that aggregates the extracted features into a more compact form using 256 neurons and ReLU activation. Ultimately, the output is flattened into a one-dimensional vector to be combined with a final prediction or pipeline.

$$h_{\text{flat}} = \text{Flatten}(h) \quad (21)$$

### Pipeline 3: Dressed quantum circuit

The third pipeline in TriQXNet consists of a central variational quantum circuit flanked by two classical layers (see Fig. 1 and Table 4). The core quantum circuit is "dressed" with classical preprocessing and postprocessing layers. This quantum circuit encodes the input features onto qubits and performs quantum operations to extract valuable information. The first classical layer acts as a trainable embedding block. It effectively transforms the raw input data into a format suitable for processing by a quantum circuit. The final classical layer serves as a decoding block, interpreting the outcome of the quantum computations and generating the final Dst forecasts.

A TimeDistributed dense layer with 32 neurons serves as the foundation for the dressed quantum circuit, and ReLU activation is applied individually to each timestep of the input sequence. The classical input data are processed in this layer, improving its representation for subsequent processing. The features are supplied into a dense layer with a width of  $(2^n)^3$ , where  $n$  is the total number of qubits in the quantum layer after they have been flattened. This layer ensures that the classical properties are correctly transferred into the quantum domain by acting as a link between the classical and quantum components of the model. The output of this dense layer is split into three equal parts along the feature dimension. Each part is then processed independently by a separate quantum layer, denoted as QLayer<sub>1</sub>, QLayer<sub>2</sub>, and QLayer<sub>3</sub>. After processing through the quantum layers, the outputs are concatenated along the feature dimension to reintegrate the quantum-processed features. Next, two more dense layers with 256 and 32 neurons each are applied to this concatenated feature vector, and ReLU activation functions follow. These layers further refine the representation of the integrated features, enhancing their discriminative power. Finally, the output is flattened once again to prepare it for combination with the outputs of other pipelines or final prediction.

The integration of quantum components into the classical framework of TriQXNet is facilitated through the PennyLane framework. Weight forms, which describe the architecture of quantum operations, and a QNode, which represents a quantum circuit, are part of this integration. We have adapted PennyLane’s ‘amplitude Embedding’ (AE) and ‘strongly entangling layers’ (SEL) templates to incorporate quantum processes within the QNode. To utilize the computational power of quantum computers, classical data must undergo a transformation into quantum states residing on qubits. This process, facilitated by the state preparation component AE, ensures that classical information is encoded onto qubits for quantum processing. The capability of AE to process large volumes of data with comparatively few qubits is one of its main advantages. AE offers a virtually limitless number of available amplitudes, enabling the encoding of substantial data. Notably, the relationship between the number of qubits and the features to encode follows a logarithmic scale ( $\log_2(n)$ ), ensuring that the quantum resources scale efficiently with the complexity of the dataset. This logarithmic scalability empowers each additional qubit to encode a substantial amount of information, making amplitude encoding a potent strategy for managing intricate datasets in QC. A parameterized quantum circuit consisting of an embedding circuit and a variational circuit is included in the AE mechanism (Fig. 5). An AE built to encode up to  $2^n$  information features into the amplitudes of a quantum state made up of  $n$  qubits is incorporated into the embedding circuit. In this instance, the AE may encode a maximum of  $2^4 = 16$  data features using 4 qubits ( $n = 4$ ). As an alternative,  $\lceil \log_2 N \rceil$  qubits alone can be used to encode a vector with  $N$  characteristics. These amplitudes correspond to the standardized classical datapoint  $x$  of a quantum state  $|\delta_x\rangle$  with  $n$  qubits with  $N$  dimensions.

$$|\delta_x\rangle = \sum_{i=1}^N x_i |i\rangle \quad (22)$$

The quantum state  $|\delta_x\rangle$  is represented by this equation. It is a superposition of basis states  $|i\rangle$  that are weighted by the vector  $x$ 's elements  $x_i$ . Here,  $N$  corresponds to  $2^n$ , where  $n$  is the qubit count. The variable  $x_i$  denotes the  $i$ -th element of the vector  $x$ , which could be either a float or an integer. Each basis state  $|i\rangle$  belongs to the computational basis. Notably, the vector  $x$  must be normalized according to equation (23).

$$\sum_{i=1} |x_i|^2 = 1 \quad (23)$$

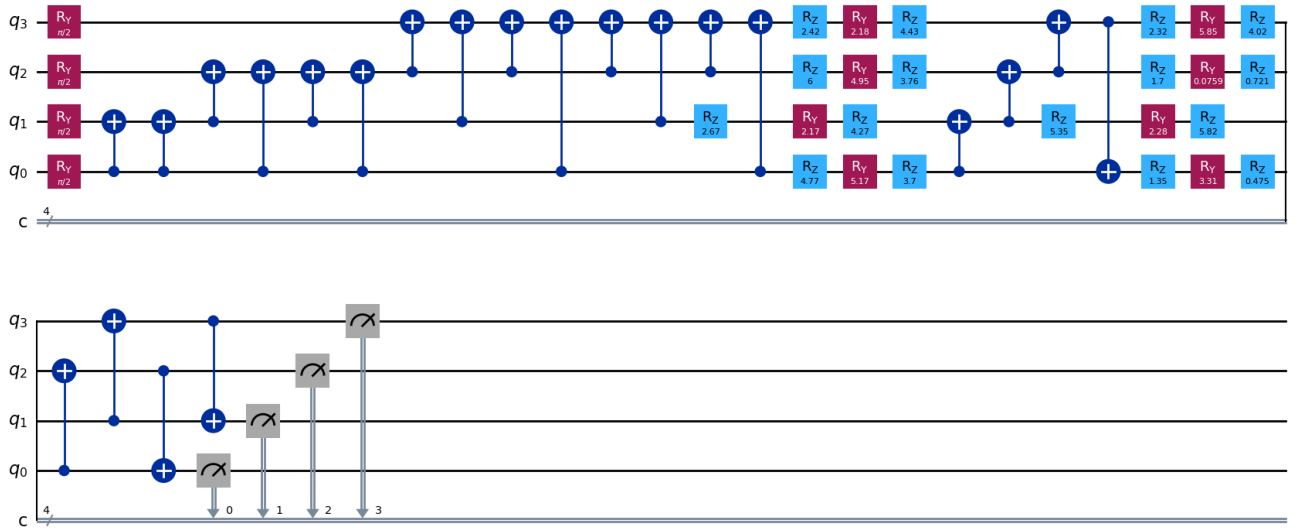


**Figure 5.** TriQXNet's quantum circuit representation consists of 4 qubits with the labels '0', '1', '2', and '3'. Two variational layers, each intended for 4 qubits, are used in the architecture. The first blue lines show how the amplitudes of the quantum state have been embedded with classical properties. This is followed by applying a layer consisting of four  $R_Y \frac{\pi}{2}$  gates (see equation (24)) to each qubit individually. These rotations place the qubits in a superposition state. Trainable U3 gates (see equation (25)) are then applied to each qubit. The specific parameters of these U3 gates are optimized during the training process. Following the first variational layer, a series of blue CNOT gates (see equation (26)) entangle specific qubits. This entanglement allows for correlations between qubits that cannot be replicated by classical mechanics and is crucial for the functionality of the network. The second variational layer mirrors the first, consisting of U3 gates applied to each qubit. The final layer comprises measurements using *Pauli* – Z operators, represented by vertical bars in the circuit. *Pauli* – Z operators measure the state of a qubit along the Z axis, resulting in either a +1 or -1 outcome [Graphics produced with PennyLane-Qiskit].

$$R_Y(\delta) = \begin{bmatrix} \cos(\delta/2) & -\sin(\delta/2) \\ \sin(\delta/2) & \cos(\delta/2) \end{bmatrix} \quad (24)$$

$$R_Z(\lambda) = \begin{bmatrix} e^{-i\lambda/2} & 0 \\ 0 & e^{i\lambda/2} \end{bmatrix} \quad (25)$$

$$CNOT = \begin{bmatrix} 1 & 0 & 0 & 0 \\ 0 & 1 & 0 & 0 \\ 0 & 0 & 0 & 1 \\ 0 & 0 & 1 & 0 \end{bmatrix} \quad (26)$$

The variational stage leverages a variable number of SELs, denoted by  $L$ . Each SEL layer introduces complexity by applying trainable rotational gates to individual qubits 0, 1, 2, and 3 within the circuit. These rotations manipulate the qubits' states, allowing the circuit to explore broader possibilities. Following the rotations, CNOT gates are employed to create entanglement between specific qubits. Entanglement fosters correlations between qubits that cannot be replicated classically. The number of SEL layers ( $L$ ) for a 4-qubit circuit can be adjusted to control the model complexity. A greater number of layers allows for more intricate computations and increases the number of trainable parameters. This component's total number of trainable parameters is  $3 \times 4 \times L$ . SEL ( $G$ ) uses a method to treat each qubit as a tiny circuit element. Each qubit is represented by a special mathematical object called a  $2 \times 2$  unitary matrix in this approach. This matrix  $G$  depends on three angles  $(\eta, \delta, \lambda)$ , all within the range of  $[0, \pi]$ . Equation (27) shows the exact form of this matrix.

$$G(\eta, \delta, \lambda) = \begin{bmatrix} e^{i\delta} \cos(\eta) & e^{i\lambda} \sin(\eta) \\ -e^{-i\lambda} \sin(\eta) & e^{-i\delta} \cos(\eta) \end{bmatrix} \quad (27)$$

While the ideal "reversible" differentiation method is not supported for SEL layers in PennyLane, the software automatically selects the most appropriate alternative for training the circuit. We use the *Pauli – Z* operation to measure the state of each qubit and extract the results from the quantum processing. The qubits are compelled by this measurement to commit to one of two states: 0 or 1. Equation (28) provides the mathematical form of the *Pauli – Z* operator.

$$\zeta_z = \begin{bmatrix} 1 & 0 \\ 0 & -1 \end{bmatrix} \quad (28)$$

The *Pauli – Z* operator measures the state of each qubit after the encoded features have been processed through the variational layers. The qubits' superposition state collapses during the measurement, leaving them in one of two states: 0 or 1. For every qubit, the *Pauli – Z* operator's expectation value, represented as  $\langle \zeta_z^i \rangle \in [-1, +1]$ , is computed, with  $i$  denoting the qubit index (equation (28)). The QNode's output, a collection of these expectation values (one for each qubit), is fed into the subsequent classical layers. These classical dense layers are trained to interpret the expectation values and generate the final Dst predictions for  $t_0$  and  $t_{+1}$  hours.

### Integration of Classical and Quantum Components

The sequential architecture of Keras allows for the easy integration of quantum and classical elements. Prior to being fed into three quantum layers, which include the QNode, the input is first processed by classical layers up to a predetermined point. The thick layer with  $2^4 \times 3$  neurons that comes before the three 4-qubit quantum layers is a crucial component of this integration. This dense layer is crucial because it sets up and transfers the necessary 48-dimensional input features to the quantum layer. The model's parameters, such as weights and biases, are trained using the Adam optimizer, which was selected due to its effective management of sparse gradients and adaptable learning rates. Because the optimization is predicated on a custom RMSE loss function, the model's prediction errors are precisely measured. Throughout the training process, these parameters are iteratively adjusted to enhance the model's performance and accuracy. The focus was ensuring that the model could effectively generalize to new, unexplored data—a capability confirmed through testing. Even though the validation loss was still significantly higher, the model managed to achieve a well-balanced fit between the training data and generalization to new cases. The model parameters were adjusted across several trial runs to maximize accuracy.

Figure 6 shows the loss curve that highlights how TriQXNet can minimize the RMSE during both training and validation. These loss curves are essential for assessing the model's capacity for making accurate forecasts on unseen data, its ability to generalize, and its learning progress.

A custom callback to reduce the learning rate and backtrack callback is employed to enhance training efficiency. This custom callback, derived from 'tf.keras.callbacks.ReduceLROnPlateau', not only reduces the learning rate when the validation loss plateaus but also backtracks to the best model weights saved thus far if no improvement is observed. This ensures that the model does not diverge due to inappropriate learning rate reductions. Before decreasing the learning rate, the callback loads the optimal model weights and analyzes the validation loss metric in terms of the RMSE. If no improvement is seen after five epochs, the learning rate is reduced by a factor of 0.5. Model checkpoint callback is also used to save the model weights at their best state, based on the lowest validation loss, ensuring that the best parameters are retained. The learning rate of the Adam optimizer is set to  $1 \times 10^{-3}$ , which provides both stability and quick convergence. The training performance of each model is compared to the validation split after it undergoes 100 epochs of training with a batch size of 768. These mechanisms collectively ensure that the model maintains high performance and generalizes well to new data.

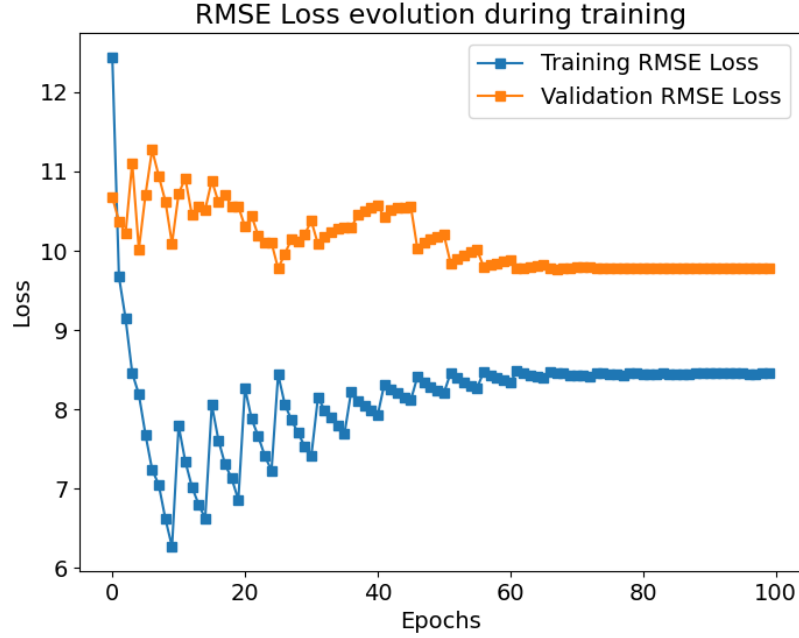


**Figure 6.** The loss evolution versus epochs for TriQXNet in Dst forecasting for  $t_0$  and  $t_{+1}$  hours is shown in this plot, which shows a consistent decrease in training and validation loss over training. This trend suggests effective learning and convergence, with minimal overfitting, as the validation loss closely follows the training loss. The capacity of TriQXNet to generalize well to new data is demonstrated by the steady decline in loss values, which strikes a compromise between fitting the training data and preserving the forecasting accuracy for future occurrences.

## Results

### Model evaluation metric

In our investigation, we sought a clear and interpretable metric to gauge the effectiveness of the constructed models. As a result, we decided to use the root mean squared error, or RMSE, of the differences in the observed and predicted Dst values.  $(y_i)$  represents the observed values at the corresponding time steps, and  $(y'_i)$  represents the expected Dst values at time steps  $(t_0)$  and  $(t_{+1})$ . The entire number of data points ( $n$ ) is represented in the RMSE equation as follows:

$$\text{RMSE} = \sqrt{\frac{1}{n} \sum_{i=1}^n (y'_i - y_i)^2} \quad (29)$$

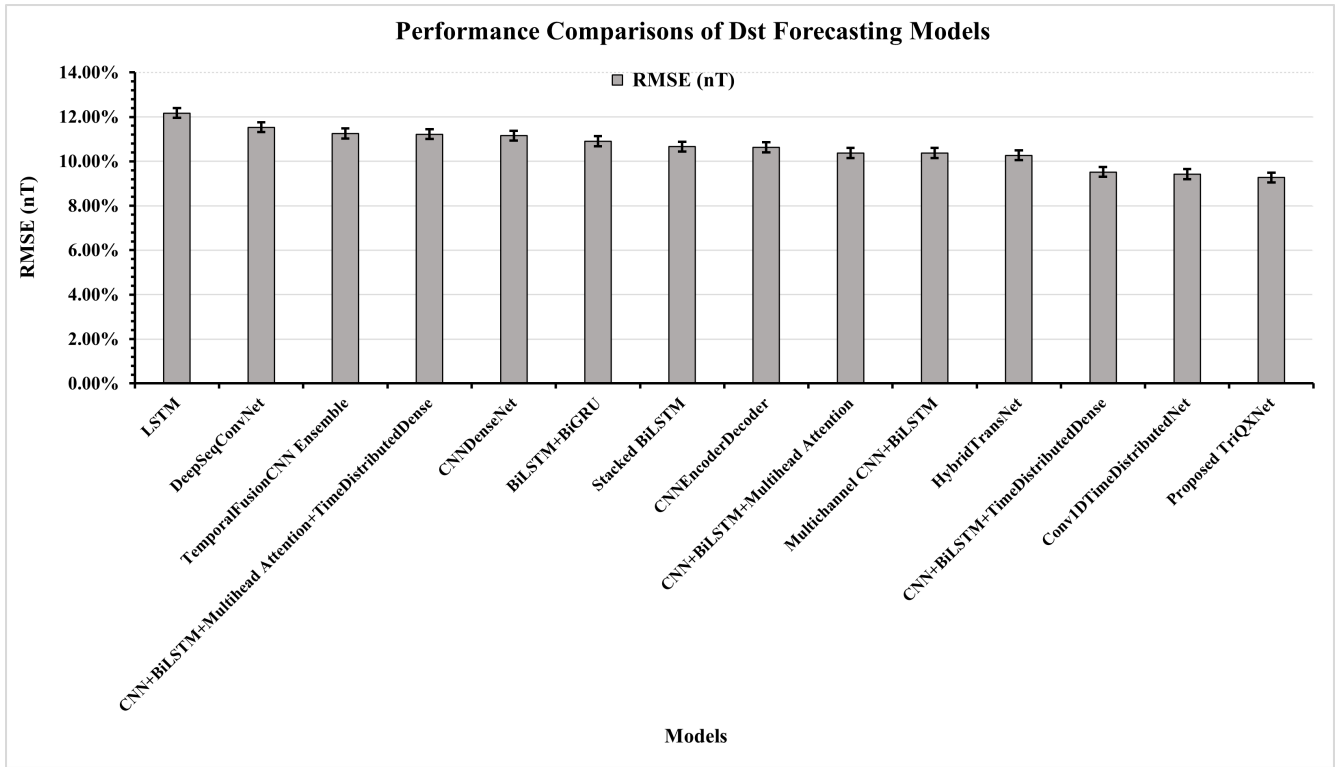
It is acknowledged that many error metrics exist; however, our selection of the RMSE was driven by several compelling factors<sup>23</sup>. The heightened sensitivity of the RMSE to outlying and significant events aligns well with our research objectives. By squaring the discrepancies, the RMSE inherently places greater weight on substantial deviations, which is particularly relevant because large errors can significantly influence model efficacy. Additionally, the extensive adoption of RMSE within scientific publications facilitates the comparison of our model's performance with prior findings. Furthermore, the RMSE gauges the average error in the same units as the dependent variable, fostering a straightforward interpretation of the model's effectiveness. Finally, as a differentiable function, the RMSE is compatible with deep learning algorithms that leverage gradient descent for parameter optimization. Because of this property, it's a favorable loss function for algorithms that use gradient descent to minimize error.

### Comparative performance benchmarking

Table 5 and Fig. 7 illustrate the comparative performance benchmarking findings, which unambiguously reveal that our proposed TriQXNet model outperforms other models in forecasting geomagnetic disturbances, as assessed by the RMSE in nT. TriQXNet outperforms all the other models in the benchmarking experiments, with an RMSE of 9.27 nT.

**Table 5.** Performance benchmarking of the models developed in this research

Model	RMSE (nT)
LSTM	12.17
DeepSeqConvNet	11.53
TemporalFusionCNN Ensemble	11.25
CNN+BiLSTM+Multihead Attention+TimeDistributedDense	11.22
CNNDenseNet	11.15
BiLSTM+BiGRU	10.90
Stacked BiLSTM	10.66
CNNEncoderDecoder	10.63
CNN+BiLSTM+Multihead Attention	10.37
Multichannel CNN+BiLSTM	10.37
HybridTransNet	12.92
CNN+BiLSTM+TimeDistributedDense	9.52
Conv1DTimeDistributedNet	9.42
<b>Proposed TriQXNet</b>	<b>9.27</b>

**Figure 7.** RMSE values for the benchmarked models for all test periods, arranged in descending order (lower values indicate better performance on the vertical axes).

Among the benchmarked models, the LSTM model exhibits the highest RMSE at 12.17 nT, indicating its relatively lower efficacy in capturing the complex temporal dependencies in the data. The DeepSeqConvNet and TemporalFusionCNN Ensemble have RMSEs of 11.53 nT and 11.25 nT, respectively. While incorporating temporal fusion and deep sequence convolution, these models appear less adept at handling the intricate patterns present in solar wind data compared to more advanced architectures. The CNN+BiLSTM+Multihead Attention+TimeDistributedDense model, with an RMSE of 11.22 nT, integrates multihead attention mechanisms to enhance feature extraction but still falls short in comparison to the more sophisticated temporal and spatial feature extraction capabilities of our proposed model. Similarly, CNNDenseNet achieves an RMSE of 11.15 nT, highlighting the limitations of relying predominantly on dense connections without adequately capturing

temporal dependencies.

As we move towards better-performing models, the BiLSTM+BiGRU (10.90 nT) and stacked BiLSTM (10.66 nT) show improvements, leveraging bidirectional recurrent layers to capture forward and backward temporal dependencies more effectively. However, their performance still has not reached the level of TriQXNet. The CNNEncoderDecoder model, with an RMSE of 10.63 nT, utilizes an encoder-decoder architecture for sequence learning but lacks the depth of feature extraction achieved by TriQXNet. Both the CNN+BiLSTM+Multihead Attention (10.37 nT) and Multichannel CNN+BiLSTM (10.37 nT) models exhibit identical RMSEs, incorporating multihead attention and multichannel convolutions, respectively. However, they do not surpass the integration of classical and quantum components in TriQXNet. The HybridTransNet model achieves a notable RMSE of 10.27 nT, reflecting its hybrid nature and potential to capture intricate temporal patterns. However, it still underperforms relative to TriQXNet.

The CNN+BiLSTM+TimeDistributedDense and Conv1DTimeDistributedNet models, with RMSEs of 9.52 nT and 9.42 nT, respectively, showcase significant improvements by integrating convolutional layers with bidirectional LSTMs and dense layers. Despite these advancements, their performance remains slightly below that of TriQXNet. Nevertheless, these hybrid models represent two crucial components of TriQXNet, providing insightful ablation test results for evaluating its effectiveness.

The RMSE of TriQXNet of 9.27 nT represents a substantial improvement over these models because of its innovative architecture comprising three distinct parallel pipelines: a classical modified Conv1DTimeDistributedNet, a classical modified CNN+BiLSTM+TimeDistributedDense, and a dressed quantum circuit. Each component in TriQXNet is designed to address the specific shortcomings of its predecessors.

The exceptional performance of TriQXNet, with an RMSE of 9.27 nT, is a result of its sophisticated architecture that combines classical deep learning techniques with QC advantages. Each component in TriQXNet is meticulously designed to capture different aspects of the input data, ensuring a comprehensive feature extraction process that outperforms its predecessors and other benchmarked models.

## Statistical validation

This section presents a statistical validation using 10-fold cross-validated paired t-tests to compare the performance of our proposed TriQXNet model against other developed models for Dst forecasting. The null hypothesis ( $H_0$ ) and alternative hypothesis ( $H_1$ ) for each comparison are as follows:

- $H_0$ : The RMSE of the TriQXNet model and its counterpart model do not significantly differ from one another.
- $H_1$ : The RMSE of the TriQXNet model and its counterpart model significantly differ from one another.

**Table 6.** 10-fold cross-validated paired t-test results between TriQXNet and the other advanced models

Model	$t$ value (RMSE)	$p$ value (RMSE)
LSTM	222.8904	3.75E-18
DeepSeqConvNet	267.9707	7.14E-19
TemporalFusionCNN Ensemble	183.396	2.17E-17
CNN+BiLSTM+Multihead Attention+TimeDistributedDense	168.4036	4.67E-17
CNNDenseNet	255.0266	1.12E-18
BiLSTM+BiGRU	204.5581	8.11E-18
Stacked BiLSTM	102.5206	4.06E-15
CNNEncoderDecoder	208.5916	6.81E-18
CNN+BiLSTM+Multihead Attention	85.22025	2.14E-14
Multichannel CNN+BiLSTM	138.0504	2.79E-16
HybridTransNet	77.832	4.83E-14
CNN+BiLSTM+TimeDistributedDense	23.43647	2.23E-09
Conv1DTimeDistributedNet	12.45518	5.60E-07

We calculated the absolute differences in the RMSE between the TriQXNet model and each counterpart for each cross-validation fold. Subsequently, paired  $t$  tests were performed using these differences to assess significance. The t-statistic and corresponding  $p$  value were computed for each comparison. We rejected  $H_0$  and came to the conclusion that there was a significant difference in the RMSE if the  $p$  value was less than the predetermined significance level ( $\alpha = 0.05$ ). Conversely, if the  $p$  value exceeded  $\alpha$ , we failed to reject  $H_0$ , indicating no significant difference in the RMSE.

The 10-fold cross-validated paired  $t$  test results revealed significant differences in the RMSE between the TriQXNet model and all the other models examined. For instance, the TriQXNet model showed a significantly lower RMSE than the LSTM



model ( $t = 222.89$ ,  $p < 0.05$ ). Similarly, significant differences were observed when comparing the TriQXNet model with DeepSeqConvNet ( $t = 267.97$ ,  $p < 0.05$ ), TemporalFusionCNN Ensemble ( $t = 183.40$ ,  $p < 0.05$ ), and other models. These findings provide robust evidence of the superiority of the TriQXNet model in terms of its predictive accuracy over its existing counterparts.

We confirm the performance of TriQXNet in Dst forecasting and emphasize its potential to advance the state-of-the-art in the field with our 10-fold cross-validated paired t-tests, which show that it outperforms other models in terms of the RMSE.

### Conformal prediction analysis

We flattened the test, validation, and training datasets to ensure compatibility with the ‘crepes’ framework<sup>49</sup>. The flattening process converts the multidimensional arrays into a 2D format suitable for subsequent analysis. The datasets are then reshaped, maintaining the time-step dimension and ensuring consistent model training and evaluation input sizes.

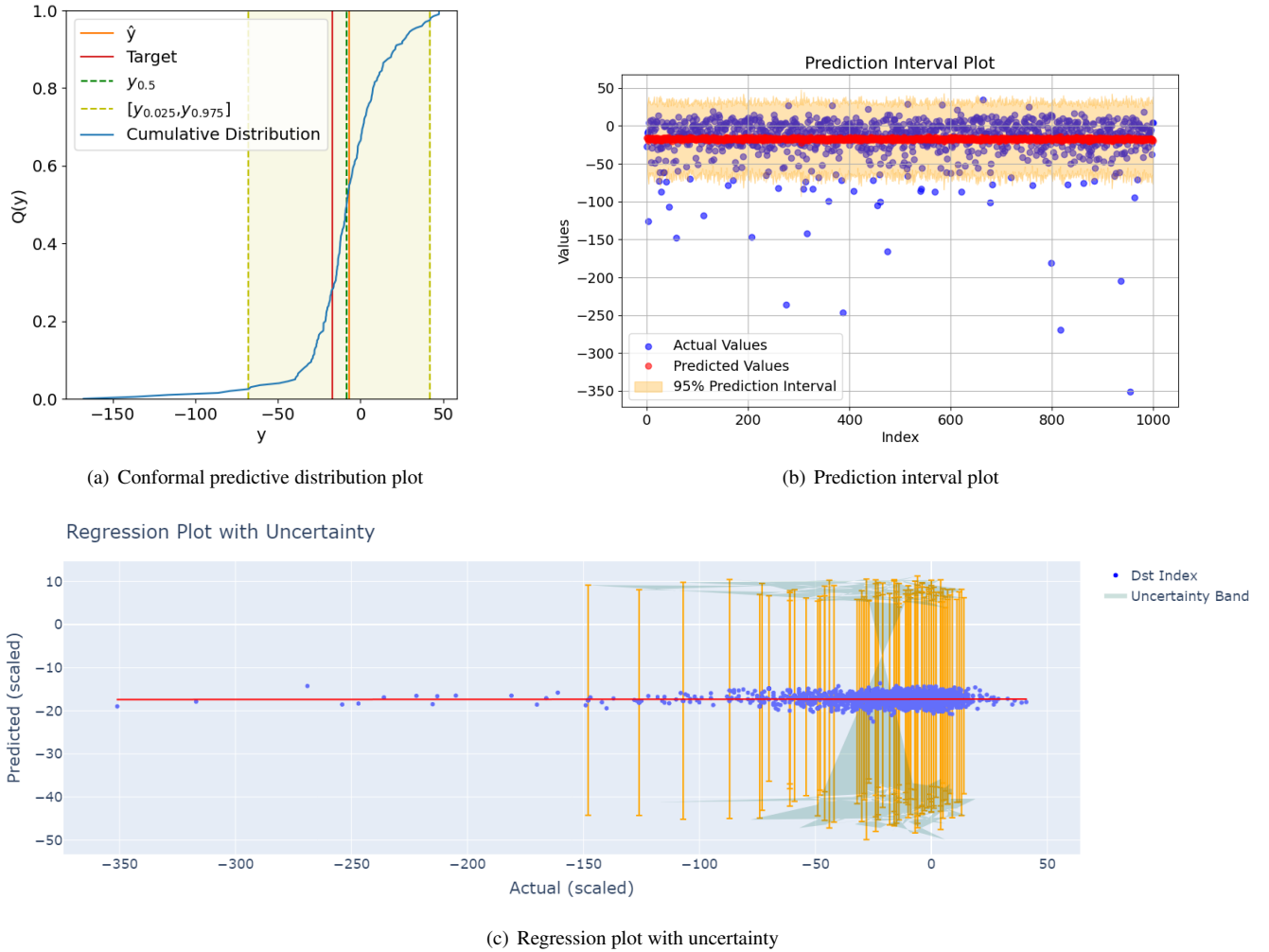


**Figure 8.** (a) Conformal predictive distribution for a randomly selected test instance. (b) The scatter plot displays the actual values (in blue) against their predicted counterparts (in red) for the first 1000 data points, offering a direct comparison between the observed and forecasted values. The orange-shaded area represents the 95% prediction interval. (c) The scatter plot illustrates the relationship between the actual Dst index values and the predicted values overlaid with a trendline and uncertainty bands.

We used the conformal predictive system (CPS) to generate prediction intervals, focusing on standard and difficulty-based normalization techniques. Using the residuals from the calibration set, we created a standard conformal regressor to generate prediction intervals with a 99% confidence level. The intervals were adjusted to exclude impossible values (those below 0 and

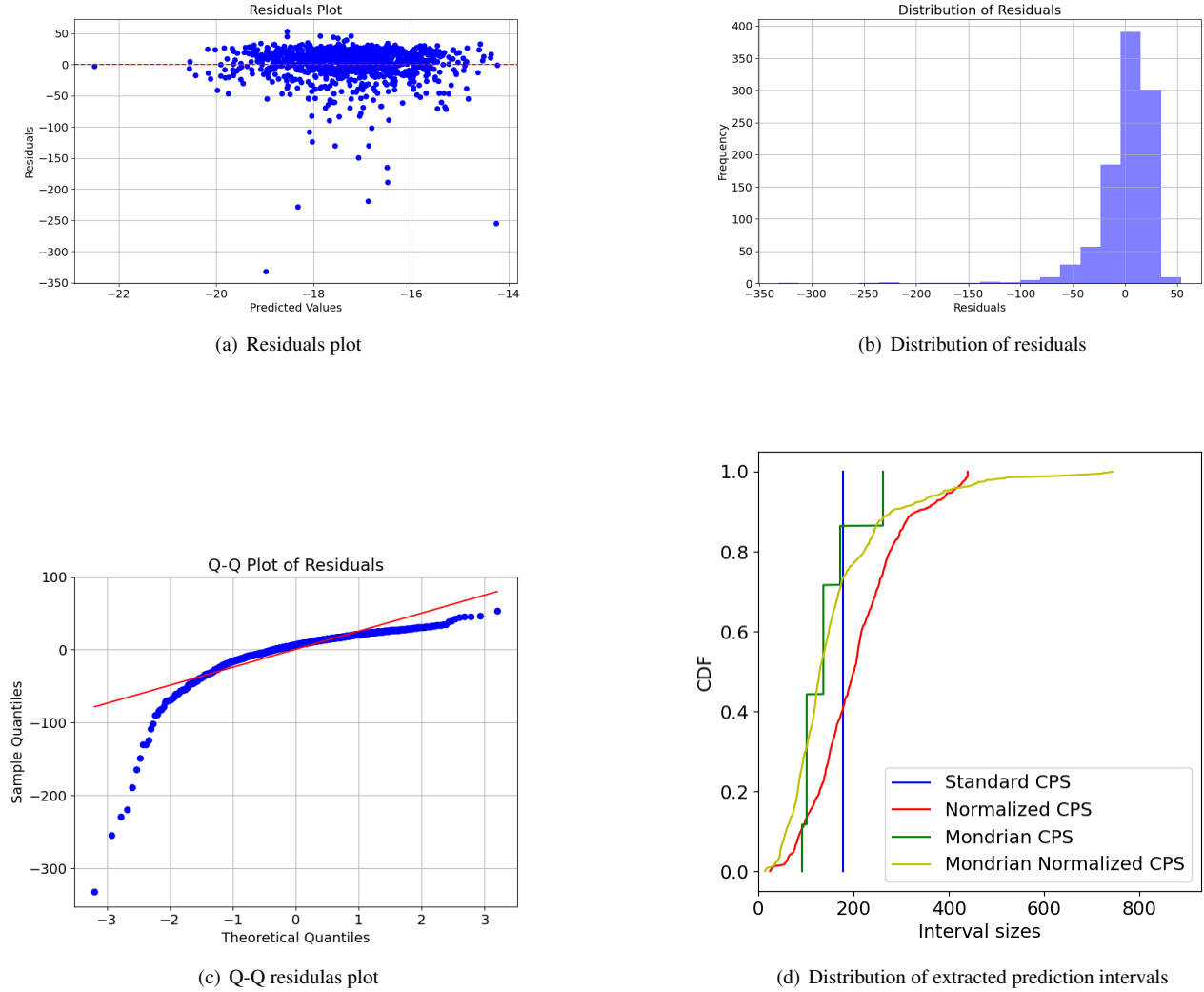


**Figure 9.** (a) This residual plot illustrates the differences (residuals) between the expected and actual values. (b) This graphic illustrates the residuals’ histogram, which sheds light on their distribution. (c) An x-axis showing the theoretical quantiles of a standard normal distribution and a y-axis showing the sample quantiles of the residuals is displayed in the quantile-quantile (Q-Q) plot of the residuals versus a normal distribution. (d) The fraction of intervals within each size range and the sorted sizes of prediction intervals are displayed, with each line denoting a distinct CP method. Standard approaches are shown by dotted lines, and standard methods are indicated by solid lines. The cumulative distribution is represented by the y-axis, while the interval sizes are displayed on the x-axis.

above 1), further tightening the predictions. We implemented a difficulty estimator based on k-nearest neighbors (k-NN) to scale the residuals, producing more informative intervals. The difficulty estimates, denoted as  $\sigma$ , were integrated into the conformal regressor to account for varying data complexities. We employed Mondrian conformal regressors, which generate prediction intervals by categorizing the data into nonoverlapping bins based on difficulty estimates. We constructed and fitted standard and normalized CPSs. The standard CPS utilized residuals from the calibration set, while the normalized CPS incorporated difficulty estimates for enhanced accuracy. We also developed Mondrian CPS by binning predictions and using these categories to normalize the CPS within each bin. This approach leverages the residuals and difficulty estimates to provide robust prediction intervals for test instances. We evaluated the predictive performance of the CPS models by analyzing the uniformity of  $p$  values for test targets and comparing prediction intervals. The results demonstrated the efficacy of the conformal prediction approaches, with the Mondrian normalized CPS providing the most reliable intervals. Finally, we visualized the conformal predictive distribution for a randomly selected test instance, plotting the cumulative distribution function and associated prediction intervals. This visualization highlights the effectiveness of our conformal prediction framework in generating accurate and

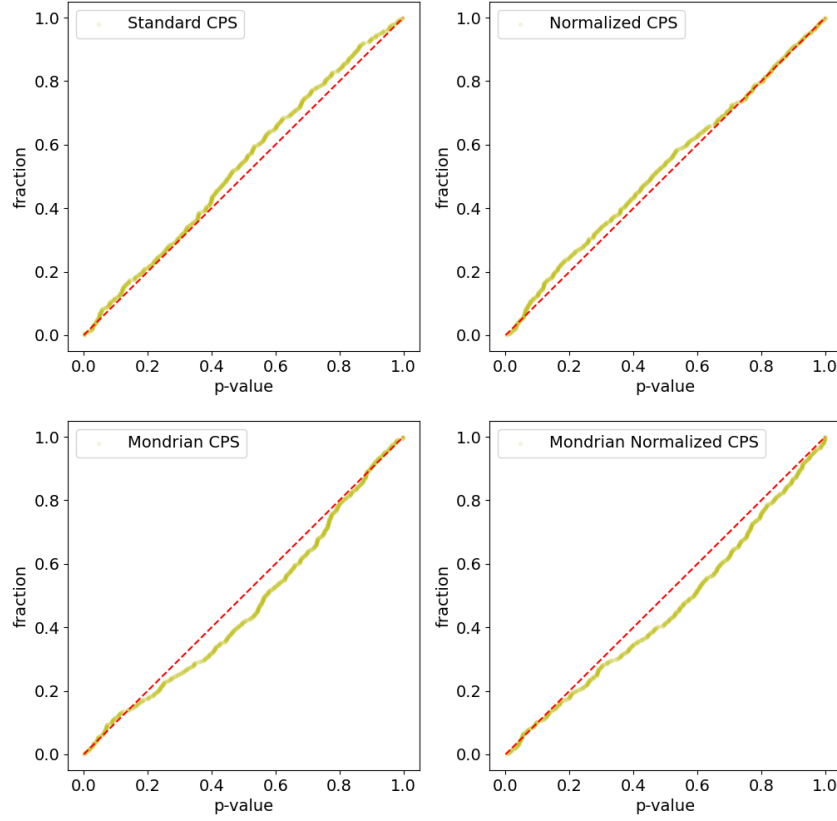


**Figure 10.** This figure displays scatter plots of sorted  $p$  values against their expected uniform distribution, comparing four CPSs used in TriQXNet, including standard CPS, normalized CPS, and Mondrian CPS. The  $p$  values are plotted on the x-axis, while the cumulative fraction of these  $p$  values is plotted on the y-axis. An ideal model would produce  $p$  values that follow a uniform distribution, depicted by the red dashed line ( $y = x$ ).

informative prediction intervals for complex datasets.

Figure 8(a) illustrates the conformal predictive distribution (CPD) for a randomly selected test instance using the Mondrian normalized CPS. The plot shows the cumulative distribution function (CDF) of the predicted values, providing a detailed view of TriQXNet’s uncertainty in Dst forecasting. Key percentiles are highlighted: the 2.5th percentile (lower bound) and the 97.5th percentile (upper bound), marking the prediction interval where the true value is expected to lie with 95% confidence. The median (50th percentile) is also indicated, showing the central tendency of the prediction. The true target value is plotted for comparison, allowing us to see how well the prediction interval captures the actual outcome. A rectangle visually represents the range between the lower and upper percentiles, highlighting the interval’s breadth. The interval in Fig. 8(b) indicates the range within which we expect the true values to lie with 95% confidence, calculated as predicted Dst values  $\pm 1.96 \times \sigma$ , where the prediction standard deviation is indicated by  $\sigma$ . Figure 8(c) shows how well the model’s predictions align with the actual values, with the trendline providing a visual indication of the linear fit. Error bars on a subset of data points represent each prediction’s predicted uncertainties ( $\sigma$ ), highlighting the prediction’s variability and confidence. The shaded band represents the uncertainty interval  $\hat{y}_i \pm \sigma_i$ , where  $\hat{y}_i$  is the predicted value for the  $i$ -th observation and  $\sigma_i$  is the standard deviation of the prediction uncertainty for the  $i$ -th observation.

By plotting the residuals against the predicted values, Fig. 9(a) helps identify any systematic errors in the TriQXNet predictions. Ideally, the residuals should be randomly distributed around zero, indicating that the TriQXNet captures the underlying data structure well without systematic bias. A red dashed line at zero aids in visually assessing this criterion. The

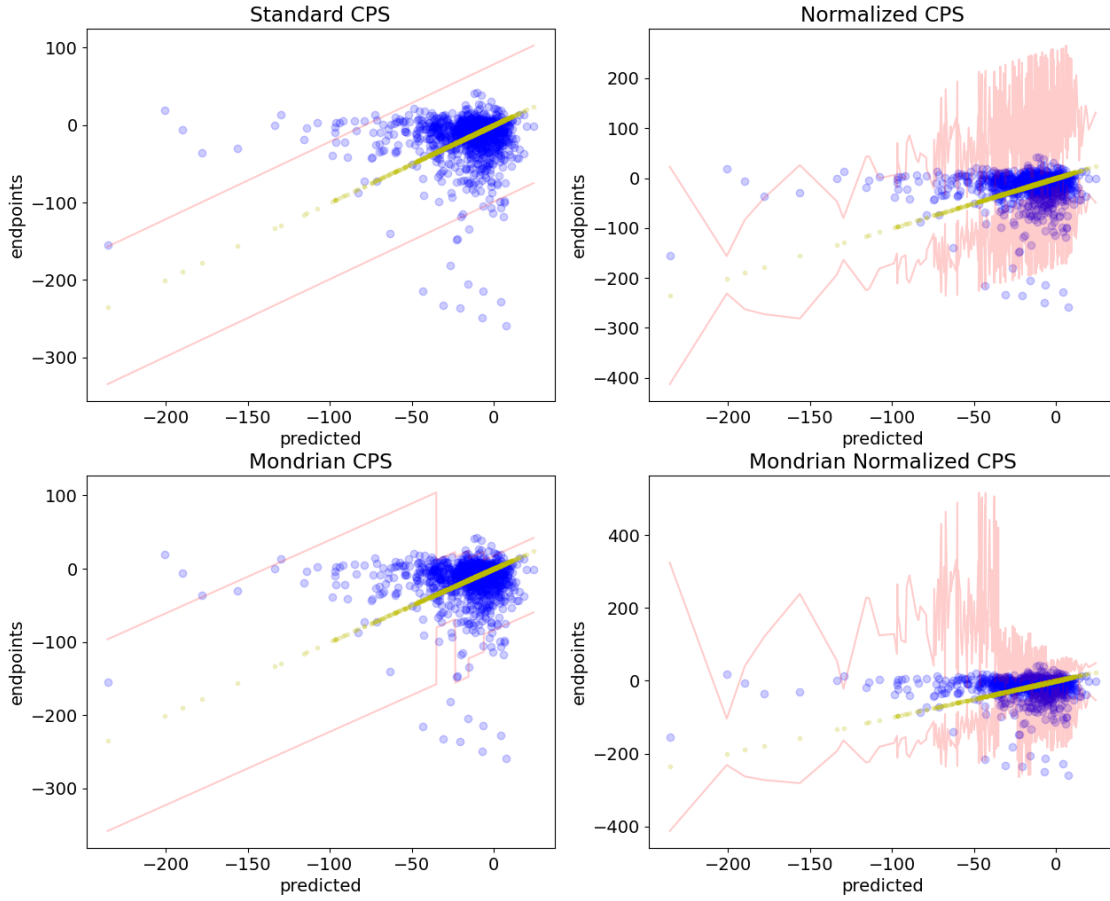


**Figure 11.** Predicted intervals for the conformal predictive systems, including standard CPS, normalized CPS, Mondrian CPS, and Mondrian normalized CPS (from top left to right). In each subplot, the x-axis represents the predicted values, while the y-axis shows the corresponding prediction interval bounds. The red lines indicate these intervals' upper and lower bounds, illustrating the range within which the true Dst values are expected to decrease. The blue dots indicate the actual observed Dst values, providing a direct visual comparison between the predicted intervals and real outcomes. Yellow dots, positioned at the center of the intervals, denote the predicted values.

normal distribution of residuals in Fig. 9(b) suggests that the model's errors are random and unbiased, a desirable property in predictive modeling. The frequency of residuals around zero further confirms TriQXNet's accuracy. This plot is necessary for validating the assumption of normality in residuals, which underpins many statistical tests and model evaluation metrics. In case the residuals exhibit a normal distribution, the points ought to be situated roughly along the reference line (a 45° line through the origin), as shown in Fig. 9(c). Deviations from this line indicate departures from normality, which can suggest issues such as skewness or kurtosis in the residuals. Figure 9(d) illustrates the CDFs of prediction interval sizes for the four CPSs implemented in our test split with lower percentiles (2.5%) and higher percentiles (97.5%).

In Fig. 10, the  $p$  values are denoted as  $p_i = \Pr(Y_i \leq \hat{y}_i)$ , where  $Y_i$  is the random variable representing the true Dst value and  $\hat{y}_i$  is the predicted Dst for the  $i$ -th test instance. Deviations from the  $y = x$  line indicate miscalibration, where the prediction intervals might be too wide or too narrow.

Figure 11 compares the prediction intervals generated by four different CPSs as applied to Dst forecasting. This layout demonstrates how accurately the CPS models capture the true Dst values within their prediction intervals. The consistent central positioning of the yellow dots relative to the interval bounds confirms that the predictions are unbiased and symmetrically

distributed around the observed values. Evaluating the width and consistency of these intervals across different CPS models is crucial, as narrower and more accurate intervals signify greater reliability of TriQXNet.

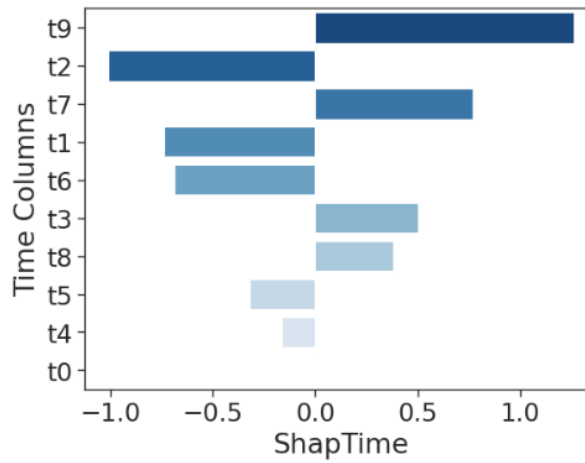
### XAI interpretation

We implemented ShapTime and PFI, both model-agnostic XAI techniques, to elucidate the black-box nature of the TriQXNet model.

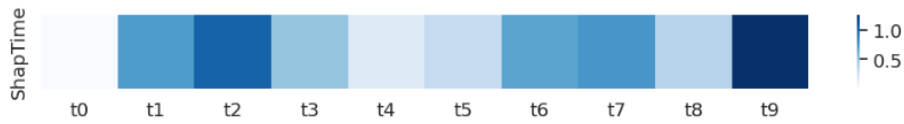
#### ShapTime

To understand how different features contribute to TriQXNet's predictions, we employed ShapTime, a technique that explains model behavior. We set the number of time periods considered (called "supertimes") to 10, resulting in the model expressed by equation (30). This equation shows how the predicted value ( $y_t$ ) is influenced by the contributions of each super-time ( $t_0$  to  $t_9$ ) and an error term ( $\omega_t$ ).

$$y_t = \delta_{t_0}t_0 + \delta_{t_1}t_1 + \dots + \delta_{t_9}t_9 + \omega_t \quad (30)$$



(a) ShapTime bar plot showing features' relative contributions to the TriQXNet predictions in descending order.



(b) ShapTime heatmap showing the variation in feature contribution over time in TriQXNet.

**Figure 12.** Evaluation of the ShapTime results for the proposed TriQXNet model.

The analysis revealed that the most recent supertime ( $t_9$ ) strongly impacts TriQXNet's predictions, while the earliest ( $t_0$ ) has the least influence. This is visualized in Fig. 12(a) (a bar plot illustrating the average SHAP values for each feature in TriQXNet) and Fig. 12(b) (a heatmap). The heatmap in Fig. 12(b) goes a step further by showing how the importance of each feature changes over time. This allows us to see how TriQXNet relies on different features at different points in the time series.

The stability of ShapTime's explanations is crucial because they build trust in our proposed TriQXNet model. Consistent explanations across different models and datasets make it easier for users to understand how the model works. In contrast, if explanations vary significantly, users might become skeptical or abandon the model altogether. We could theoretically perturb the training data based on the ShapTime results to further demonstrate the importance of these supertimes. For example, we could swap a critical supertime with a less important one. We expect this to significantly deteriorate TriQXNet's performance. In our case, this point can be illustrated by replacing the crucial  $t_9$  with the least influential  $t_0$  and  $t_2$  with  $t_4$ . This approach is similar to sensitivity analysis, a common technique in XAI.

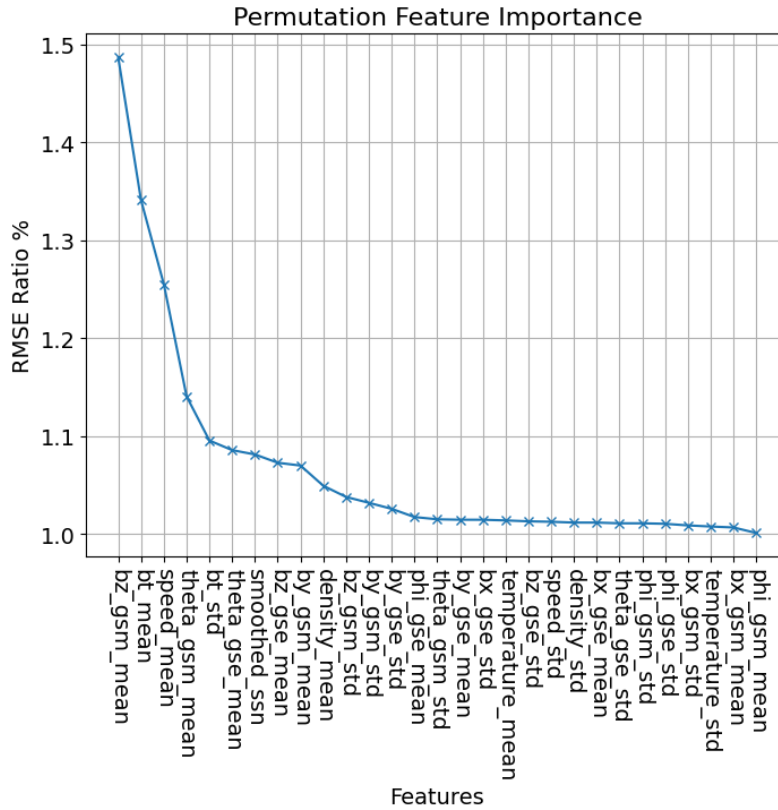


**Figure 13.** Plot of PFI analysis conducted on our TriQXNet model. The y-axis represents the relative significance of each feature, expressed as the ratio of the RMSE for a specific feature compared to the RMSE obtained using the most important feature ("bz\_gsm\_mean"). Higher ratios on the y-axis indicate features that contribute more significantly to the model's prediction accuracy.

### Permutation feature importance

To understand how different features influence TriQXNet's ability to forecast the Dst index, we conducted a permutation feature importance (PFI) analysis (see Fig. 13). In the PFI, the importance of a feature is measured by the amount that the model performance worsens when the order of that feature's values is shuffled. Features with higher PFI scores contribute more significantly to the accuracy of forecasts.

Our analysis reveals that the "bz\_gsm\_mean" feature, with a PFI of 1.49%, is the most influential predictor of the Dst index. This implies that a key factor influencing our model predictions is the average geomagnetic field value in the GSM coordinate system. Other important features include "bt\_mean" (1.34%), "speed\_mean" (1.25%), "theta\_gsm\_mean" (1.14%), and "bt\_std" (1.09%). These features likely capture aspects of the IMF, solar wind speed, and the angle of the IMF in the GSM coordinate system, all of which are known to influence geomagnetic activity.

## Discussion

This study represents a notable advancement in applying QC to space weather forecasting, a domain with a large amount of research yet critical importance due to the potentially severe impacts of geomagnetic storms on satellites, power grids, and communications systems. Despite extensive research on Dst forecasting, comparing prediction methods is challenging due to variations in data subsets, computational platforms, and optimization for specific solar cycles. Three main challenges arise when applying these models in real-time: (a) relying on historical Dst values, which are frequently imprecise and delayed; (b) using time-shifted and processed NASA OMNI data, which differs from the noisier, real-time RTSW data collected by NASA's ACE and NOAA's DSCOVR satellites; and (c) having to run the models within constrained, operationally approved computational resources using RTSW data streams. As a result, reliable real-time Dst prediction models must be independent of previous Dst values, able to deal with noise and missing data in RTSW data, and able to work in particular operational computing environments. To close these gaps, we present a novel theoretical framework that integrates classical and QC



methods, conformal prediction, and XAI within hybrid deep neural networks, setting a new standard in the field.

We compared our performance against those of previous studies using the same dataset to test the practical effectiveness of TriQXNet in Table 7. The architecture and complexity of the models and methods from these studies differ greatly, which has an effect on their processing needs and predictive performance. The RMSE was improved to 10.60 nT by Nair et al. from NOAA using an ensemble of four state-of-the-art models, but this improvement came at the expense of a very high parameter count of 62.69 million, demonstrating the significant computational resources needed for this ensemble technique. Their model is also utilized by the CIRES/NCEI geomagnetism team on their website as the official geomagnetic model of NOAA (<https://geomag.colorado.edu/dst-predict>). In contrast, our proposed TriQXNet model achieves a superior RMSE of 9.27 nT, outperforming all previous models. TriQXNet accomplishes this with a parameter count of 395,578, which is significantly lower than that of many of the well-performing models. This demonstrates that TriQXNet provides better predictive accuracy and offers a more efficient and scalable solution in terms of computational resources.

**Table 7.** Performance comparison with previous recent studies on the same dataset

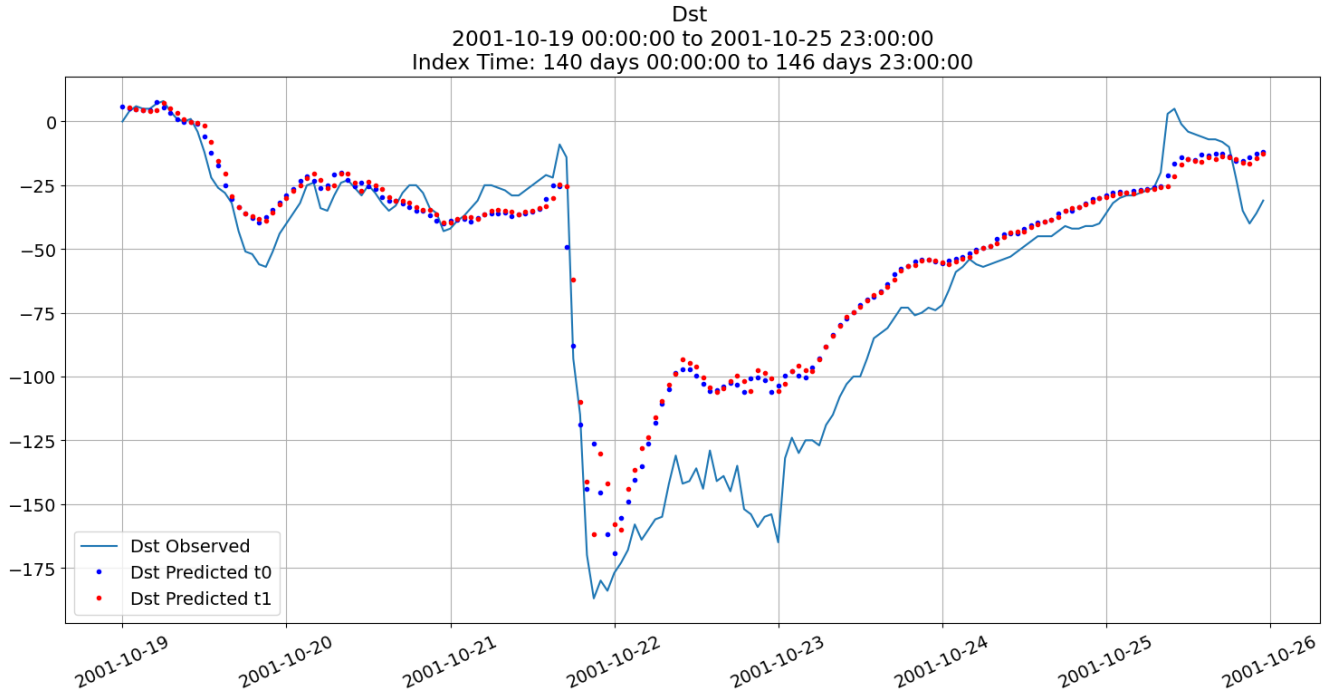
Reference(s)	Model/Approach	RMSE (nT)	Number of parameters
Ali (2021) <sup>19</sup>	M1: A model combining BiLSTM and BiGRU with 3 flattening layers and 3 dense layers	11.13	60 million
Trotta (2021) <sup>19</sup>	M2: An ensemble consisting of 5 CNNs	11.25	51,191
Medina and Medina (2021) <sup>19</sup>	M3: An ensemble composed of 1 LightGBM model and 2 FFNs	11.30	34,354
Eissa and Amer (2021) <sup>19</sup>	M4: An ensemble of 21 CNNs, each with 4 blocks	11.53	2.6 million
Nair et al. (2023) <sup>18</sup>	An ensemble combining M1, M2, M3, and M4 models	10.60	62.69 million
<b>Ours</b>	<b>Proposed TriQXNet</b>	<b>9.27</b>	<b>3,95,578</b>

Figure 14 describes the user's selection of a specific extreme event case study where the observed Dst declined rapidly and the subsequent prediction of Dst using our proposed TriQXNet. We defined the 140th day as the starting point for the event, and the RMSE for predictions at  $t_0$  was found to be 20.33 nT, while at  $t_{+1}$ , it was 20.86 nT. These results imply that, despite some variations between the expected and observed values, TriQXNet's predictions were generally accurate. For example, on October 22, 23, and 24, the observed Dst index was lower than the values predicted by TriQXNet. Accurately predicting extreme negative Dst values is crucial due to the severe real-world implications of geomagnetic storms. These storms can induce harmful electrical currents in satellites, leading to damage or destruction and affecting power grids, potentially causing widespread blackouts. Additionally, geomagnetic storms can interfere with radio communications, posing risks to aviation safety. Given these potential impacts, the ability of TriQXNet to predict Dst with relatively low error demonstrates its effectiveness and reliability in forecasting such critical space weather events. Our model, TriQXNet, mitigates these risks by providing more reliable forecasts, demonstrating the practical benefits of QC in tackling complex real-world problems.

One of the unique contributions of our research is the integration of explainable classical–quantum neural networks with quantifiable uncertainty for enhanced geomagnetic storm prediction. This approach harnesses the computational power of quantum mechanics, combined with classical neural network architectures, to handle the complex, nonlinear relationships inherent in solar wind and geomagnetic data. This fusion has been attempted for the first time in our study and has shown promising results, pushing the boundaries of the current space weather forecasting methodologies. Implementing TriQXNet in real-world applications represents a significant milestone in advancing modern QC technology. By demonstrating its superior performance compared to advanced deep learning models and NOAA's own prediction methods, we have provided concrete evidence of the practical benefits of classical–quantum techniques. This opens up new avenues for further QC research and establishes a new standard for space weather prediction.

Our model's performance has important implications for various sectors reliant on accurate space weather forecasting. For satellite operators, enhanced prediction accuracy can help mitigate the risks associated with geomagnetic storms, extend the operational life of satellites, and reduce maintenance costs. Power grid operators can use these forecasts to prepare for potential disruptions, preventing large-scale blackouts and maintaining grid stability. Moreover, improved prediction accuracy can significantly enhance aviation safety by ensuring reliable communication and navigation systems.

The future scope of this research is vast and includes integrating TriQXNet into operational forecasting systems, expanding datasets to encompass longer time ranges for more comprehensive forecasting, and further exploring the potential of more complex classical–quantum neural network architectures. These efforts will ensure that space weather predictions continue to evolve, becoming more accurate and reliable, thus safeguarding critical technological infrastructures and reducing the economic impact of geomagnetic storms.



**Figure 14.** This plot illustrates the Dst values predicted and observed by TriQXNet between 19 and 25 October 2001. The y-axis represents the Dst index. Currents that are directed northward are indicated by negative values, and those that are directed southward by positive values. Larger magnitudes indicate stronger storms. The x-axis denotes a period of 7 days. The minimum Dst observed was approximately -180 nT during this period.

This research demonstrates the transformative potential of hybrid classical–quantum approaches and significantly advances the field of QC by applying it to a critical and complex application. Our study emphasizes the need for ongoing research and development in Dst forecasting and the wider applications of quantum machine learning, as demonstrated by our model’s superior performance over sophisticated deep learning models and the prediction techniques currently employed by NOAA. This work contributes substantially to the advancement of modern QC technology, demonstrating its practical utility and paving the way for future innovations in space weather prediction and beyond.

## Conclusions

This study marks a pioneering application of QC in space weather forecasting, representing a significant leap forward in leveraging QC for astronomical phenomena. We introduce a novel theoretical framework combining classical and QC methods, conformal prediction, and XAI with hybrid neural networks, setting a new standard for Dst index forecasting. Our sophisticated data preprocessing pipeline, which includes feature selection, normalization, aggregation, and imputation techniques, ensures that our models have the highest quality of input data. The proposed hybrid classical–quantum neural network architecture, which features three parallel channels for processing preprocessed solar wind data, significantly enhances the robustness and accuracy of Dst index predictions. This model is designed for operational deployment and can handle real-time data streams from NASA’s ACE and NOAA’s DSCOVR satellites, ensuring our predictions are based on the most current and relevant data. The model forecasts the Dst index for both  $t_0$  and  $t_{+1}$ , providing valuable lead time for mitigating the adverse effects of geomagnetic storms. Our model’s performance is rigorously evaluated using the RMSE and compared with that of 13 hybrid deep-learning models, which outperform all the models with an RMSE of 9.27 nT. Through 10-fold cross-validated paired t-tests against all the advanced deep-learning models, we validated the significant performance of TriQXNet in terms of the RMSE, assuming  $\alpha = 5\%$ . Additionally, by implementing conformal prediction techniques, we quantify the uncertainty in our forecasts, providing confidence intervals crucial for operational decision-making. Incorporating XAI concepts such as ShapTime and PFI further enhances the interpretability of our model, making it easier for users to understand and trust its predictions.

Even though our study has significantly improved Dst forecasting, it is crucial to recognize these limits as they provide various opportunities for further QC-based work in this area in the future. First, there is a problem with depending solely on

real-time, high-quality solar wind data from ACE and DSCOVR satellites. The accuracy of our forecasts may be impacted by noise, gaps, and spikes in these data streams, which can result from sensor failures and processing system problems. Second, the computational complexity of our hybrid classical–quantum neural network, TriQXNet, necessitates substantial computational resources. This requirement could limit the model’s operational deployment in environments with restricted computational capabilities. Additionally, integrating QC techniques, while innovative, introduces complexities that must be managed to ensure reliable and efficient operation. Third, the forecasts made by our model at this time are limited to the short term, that is the Dst index for the next few hours. While this provides valuable immediate insights, it may not fully meet the needs of all operational scenarios that require longer-term forecasts. Furthermore, our study utilized only Amplitude Embedding for quantum data encoding. Exploring other encoding techniques in QC, such as Basis Encoding, Angle Encoding, and QSample Encoding, could enhance the model’s performance. For example, Angle Encoding could offer more granular control over the representation of input features, while Basis Encoding might provide a simpler implementation for certain data types.

## Data availability

The solar wind data from NASA’s ACE and NOAA’s DSCOVR satellites make up the public and private datasets used in this study. Public data, which include solar wind measurements from both satellites, are freely available. Through NASA’s OMNIWeb interface, solar wind observations from the ACE spacecraft are accessible. On the other hand, the National Centers for Environmental Information (NCEI), a division of the NOAA, is the source of NOAA’s DSCOVR satellite measurements. Links to the public datasets are as follows: NASA OMNIWeb (<https://omniweb.gsfc.nasa.gov/>), NASA NSSDC Data (<https://nssdc.gsfc.nasa.gov/>), NOAA DSCOVR Public and Private Data (<https://ngdc.noaa.gov/geomag/data/geomag/magnet>).

## Author contributions statement

**M.A.J.:** Conceptualization, Methodology, Data curation, Writing – Original Draft Preparation, Software, Visualization, Investigation. **M.F.M.:** Supervision, Reviewing, and Editing. **Z.A.:** Advising, Reviewing, and Editing. **N.D.:** Advising, Reviewing, and Editing. **R.S.S.:** Advising, Reviewing, and Editing.

## Competing interests

The authors have no conflicts of interest to declare that are relevant to this article.

## Additional information

Correspondence and requests for materials should be addressed to M.A.J.

## References

1. Mursula, K., Qvick, T., Holappa, L. & Asikainen, T. Magnetic Storms During the Space Age: Occurrence and Relation to Varying Solar Activity. *J. Geophys. Res. Space Phys.* **127**, e2022JA030830, DOI: [10.1029/2022JA030830](https://doi.org/10.1029/2022JA030830) (2022). [\\_eprint: https://onlinelibrary.wiley.com/doi/pdf/10.1029/2022JA030830](https://onlinelibrary.wiley.com/doi/pdf/10.1029/2022JA030830).
2. Gonzalez, W. D., Gonzalez, A. L. C. & Tsurutani, B. T. Dual-peak solar cycle distribution of intense geomagnetic storms. *Planet. Space Sci.* **38**, 181–187, DOI: [10.1016/0032-0633\(90\)90082-2](https://doi.org/10.1016/0032-0633(90)90082-2) (1990).
3. Sugiura, M. Hourly values of equatorial Dst for the IGY. Tech. Rep., National Aeronautics and Space Administration (NASA) (1963). (No. NASA-TM-X-55238).
4. Nair, M. *et al.* Next Generation High-Definition Geomagnetic Model for Wellbore Positioning, Incorporating New Crustal Magnetic Data. In *Day 4 Thu, August 19, 2021*, D041S048R005, DOI: [10.4043/31044-MS](https://doi.org/10.4043/31044-MS) (OTC, Virtual and Houston, Texas, 2021).
5. Chulliat, A., Vigneron, P. & Hulot, G. First results from the Swarm Dedicated Ionospheric Field Inversion chain. *Earth, Planets Space* **68**, 104, DOI: [10.1186/s40623-016-0481-6](https://doi.org/10.1186/s40623-016-0481-6) (2016).
6. Chulliat, A., Vigneron, P., Thébaud, E., Sirol, O. & Hulot, G. Swarm SCARF Dedicated Ionospheric Field Inversion chain. *Earth, Planets Space* **65**, 1271–1283, DOI: [10.5047/eps.2013.08.006](https://doi.org/10.5047/eps.2013.08.006) (2013).
7. Maus, S., Manoj, C., Rauberg, J., Michaelis, I. & Lühr, H. NOAA/NGDC candidate models for the 11th generation International Geomagnetic Reference Field and the concurrent release of the 6th generation Pomme magnetic model. *Earth, Planets Space* **62**, 2, DOI: [10.5047/eps.2010.07.006](https://doi.org/10.5047/eps.2010.07.006) (2010).

8. Maus, S. & Lühr, H. Signature of the quiet-time magnetospheric magnetic field and its electromagnetic induction in the rotating Earth. *Geophys. J. Int.* **162**, 755–763, DOI: [10.1111/j.1365-246X.2005.02691.x](https://doi.org/10.1111/j.1365-246X.2005.02691.x) (2005). [\\_eprint: https://onlinelibrary.wiley.com/doi/pdf/10.1111/j.1365-246X.2005.02691.x](https://onlinelibrary.wiley.com/doi/pdf/10.1111/j.1365-246X.2005.02691.x).
9. Gruet, M. A., Chandorkar, M., Sicard, A. & Camporeale, E. Multiple-Hour-Ahead Forecast of the Dst Index Using a Combination of Long Short-Term Memory Neural Network and Gaussian Process. *Space Weather*. **16**, 1882–1896, DOI: [10.1029/2018SW001898](https://doi.org/10.1029/2018SW001898) (2018). [\\_eprint: https://onlinelibrary.wiley.com/doi/pdf/10.1029/2018SW001898](https://onlinelibrary.wiley.com/doi/pdf/10.1029/2018SW001898).
10. Burton, R. K., McPherron, R. L. & Russell, C. T. An empirical relationship between interplanetary conditions and Dst. *J. Geophys. Res. (1896-1977)* **80**, 4204–4214, DOI: [10.1029/JA080i031p04204](https://doi.org/10.1029/JA080i031p04204) (1975). [\\_eprint: https://onlinelibrary.wiley.com/doi/pdf/10.1029/JA080i031p04204](https://onlinelibrary.wiley.com/doi/pdf/10.1029/JA080i031p04204).
11. Gleisner, H., Lundstedt, H. & Wintoft, P. Predicting geomagnetic storms from solar-wind data using time-delay neural networks. *Annales Geophys.* **14**, 679–686, DOI: [10.1007/s00585-996-0679-1](https://doi.org/10.1007/s00585-996-0679-1) (1996). Publisher: Copernicus GmbH.
12. Bala, R. & Reiff, P. Improvements in short-term forecasting of geomagnetic activity. *Space Weather*. **10**, DOI: [10.1029/2012SW000779](https://doi.org/10.1029/2012SW000779) (2012). [\\_eprint: https://onlinelibrary.wiley.com/doi/pdf/10.1029/2012SW000779](https://onlinelibrary.wiley.com/doi/pdf/10.1029/2012SW000779).
13. Lazzús, J. A., Vega, P., Rojas, P. & Salfate, I. Forecasting the Dst index using a swarm-optimized neural network. *Space Weather*. **15**, 1068–1089, DOI: [10.1002/2017SW001608](https://doi.org/10.1002/2017SW001608) (2017). [\\_eprint: https://onlinelibrary.wiley.com/doi/pdf/10.1002/2017SW001608](https://onlinelibrary.wiley.com/doi/pdf/10.1002/2017SW001608).
14. Chandorkar, M., Camporeale, E. & Wing, S. Probabilistic forecasting of the disturbance storm time index: An autoregressive Gaussian process approach. *Space Weather*. **15**, 1004–1019, DOI: [10.1002/2017SW001627](https://doi.org/10.1002/2017SW001627) (2017). [\\_eprint: https://onlinelibrary.wiley.com/doi/pdf/10.1002/2017SW001627](https://onlinelibrary.wiley.com/doi/pdf/10.1002/2017SW001627).
15. Xu, S. B., Huang, S. Y., Yuan, Z. G., Deng, X. H. & Jiang, K. Prediction of the Dst Index with Bagging Ensemble-learning Algorithm. *The Astrophys. J. Suppl. Ser.* **248**, 14, DOI: [10.3847/1538-4365/ab880e](https://doi.org/10.3847/1538-4365/ab880e) (2020). Publisher: The American Astronomical Society.
16. Nuraeni, F., Ruhimat, M., Aris, M. A., Ratnasari, E. A. & Purnomo, C. Development of 24 hours Dst index prediction from solar wind data and IMF Bz using NARX. *J. Physics: Conf. Ser.* **2214**, 012024, DOI: [10.1088/1742-6596/2214/1/012024](https://doi.org/10.1088/1742-6596/2214/1/012024) (2022). Publisher: IOP Publishing.
17. Nilam, B. & Ram, S. T. Forecasting Geomagnetic activity (Dst Index) using the ensemble kalman filter. *Mon. Notices Royal Astron. Soc.* **511**, 723–731, DOI: [10.1093/mnras/stac099](https://doi.org/10.1093/mnras/stac099) (2022). [\\_eprint: https://academic.oup.com/mnras/article-pdf/511/1/723/42364913/stac099.pdf](https://academic.oup.com/mnras/article-pdf/511/1/723/42364913/stac099.pdf).
18. Nair, M. *et al.* MagNet—A Data-Science Competition to Predict Disturbance Storm-Time Index (Dst) From Solar Wind Data. *Space Weather*. **21**, e2023SW003514, DOI: [10.1029/2023SW003514](https://doi.org/10.1029/2023SW003514) (2023). [\\_eprint: https://onlinelibrary.wiley.com/doi/pdf/10.1029/2023SW003514](https://onlinelibrary.wiley.com/doi/pdf/10.1029/2023SW003514).
19. Ali, A. *et al.* Winning code from the MagNet: Model the Geomagnetic Field challenge, DOI: [10.5281/zenodo.8329881](https://doi.org/10.5281/zenodo.8329881) (2021).
20. O'Brien, T. P. & McPherron, R. L. An empirical phase space analysis of ring current dynamics: Solar wind control of injection and decay. *J. Geophys. Res. Space Phys.* **105**, 7707–7719, DOI: [10.1029/1998JA000437](https://doi.org/10.1029/1998JA000437) (2000).
21. Temerin, M. & Li, X. A new model for the prediction of Dst on the basis of the solar wind. *J. Geophys. Res. Space Phys.* **107**, SMP 31–1–SMP 31–8, DOI: [10.1029/2001JA007532](https://doi.org/10.1029/2001JA007532) (2002). [\\_eprint: https://onlinelibrary.wiley.com/doi/pdf/10.1029/2001JA007532](https://onlinelibrary.wiley.com/doi/pdf/10.1029/2001JA007532).
22. Raeder, J. *et al.* Global simulation of the Geospace Environment Modeling substorm challenge event. *J. Geophys. Res. Space Phys.* **106**, 381–395, DOI: [10.1029/2000JA000605](https://doi.org/10.1029/2000JA000605) (2001). [\\_eprint: https://onlinelibrary.wiley.com/doi/pdf/10.1029/2000JA000605](https://onlinelibrary.wiley.com/doi/pdf/10.1029/2000JA000605).
23. Rastätter, L. *et al.* Geospace environment modeling 2008–2009 challenge: Dst index. *Space Weather*. **11**, 187–205, DOI: [10.1002/swe.20036](https://doi.org/10.1002/swe.20036) (2013). [\\_eprint: https://onlinelibrary.wiley.com/doi/pdf/10.1002/swe.20036](https://onlinelibrary.wiley.com/doi/pdf/10.1002/swe.20036).
24. Harrow, A. W. & Montanaro, A. Quantum computational supremacy. *Nature* **549**, 203–209, DOI: [10.1038/nature23458](https://doi.org/10.1038/nature23458) (2017). Publisher: Nature Publishing Group.
25. Dunjko, V., Taylor, J. M. & Briegel, H. J. Quantum-Enhanced Machine Learning. *Phys. Rev. Lett.* **117**, 130501, DOI: [10.1103/PhysRevLett.117.130501](https://doi.org/10.1103/PhysRevLett.117.130501) (2016). Publisher: American Physical Society.
26. Wan, K. H., Dahlsten, O., Kristjánsson, H., Gardner, R. & Kim, M. S. Quantum generalisation of feedforward neural networks. *npj Quantum Inf.* **3**, 1–8, DOI: [10.1038/s41534-017-0032-4](https://doi.org/10.1038/s41534-017-0032-4) (2017). Publisher: Nature Publishing Group.

27. Rebentrost, P., Mohseni, M. & Lloyd, S. Quantum Support Vector Machine for Big Data Classification. *Phys. Rev. Lett.* **113**, 130503, DOI: [10.1103/PhysRevLett.113.130503](https://doi.org/10.1103/PhysRevLett.113.130503) (2014). Publisher: American Physical Society.
28. Aaronson, S. Read the fine print. *Nat. Phys.* **11**, 291–293, DOI: [10.1038/nphys3272](https://doi.org/10.1038/nphys3272) (2015). Publisher: Nature Publishing Group.
29. Schetakis, N., Aghamalyan, D., Griffin, P. & Boguslavsky, M. Review of some existing QML frameworks and novel hybrid classical–quantum neural networks realising binary classification for the noisy datasets. *Sci. Reports* **12**, 11927, DOI: [10.1038/s41598-022-14876-6](https://doi.org/10.1038/s41598-022-14876-6) (2022). Publisher: Nature Publishing Group.
30. Yoshioka, N., Okubo, T., Suzuki, Y., Koizumi, Y. & Mizukami, W. Hunting for quantum-classical crossover in condensed matter problems. *npj Quantum Inf.* **10**, 1–10, DOI: [10.1038/s41534-024-00839-4](https://doi.org/10.1038/s41534-024-00839-4) (2024). Publisher: Nature Publishing Group.
31. Zhu, Y. *et al.* Flexible learning of quantum states with generative query neural networks. *Nat. Commun.* **13**, 6222, DOI: [10.1038/s41467-022-33928-z](https://doi.org/10.1038/s41467-022-33928-z) (2022). Publisher: Nature Publishing Group.
32. Heim, B., Rønnow, T. F., Isakov, S. V. & Troyer, M. Quantum versus classical annealing of Ising spin glasses. *Science* **348**, 215–217, DOI: [10.1126/science.aaa4170](https://doi.org/10.1126/science.aaa4170) (2015). Publisher: American Association for the Advancement of Science.
33. Wiebe, N., Braun, D. & Lloyd, S. Quantum Algorithm for Data Fitting. *Phys. Rev. Lett.* **109**, 050505, DOI: [10.1103/PhysRevLett.109.050505](https://doi.org/10.1103/PhysRevLett.109.050505) (2012). Publisher: American Physical Society.
34. Lloyd, S., Garnerone, S. & Zanardi, P. Quantum algorithms for topological and geometric analysis of data. *Nat. Commun.* **7**, 10138, DOI: [10.1038/ncomms10138](https://doi.org/10.1038/ncomms10138) (2016). Publisher: Nature Publishing Group.
35. Biamonte, J. *et al.* Quantum machine learning. *Nature* **549**, 195–202, DOI: [10.1038/nature23474](https://doi.org/10.1038/nature23474) (2017). Publisher: Nature Publishing Group.
36. Domingo, L., Djukic, M., Johnson, C. & Borondo, F. Binding affinity predictions with hybrid quantum-classical convolutional neural networks. *Sci. Reports* **13**, 17951, DOI: [10.1038/s41598-023-45269-y](https://doi.org/10.1038/s41598-023-45269-y) (2023). Publisher: Nature Publishing Group.
37. Chen, S. Y.-C., Wei, T.-C., Zhang, C., Yu, H. & Yoo, S. Quantum convolutional neural networks for high energy physics data analysis. *Phys. Rev. Res.* **4**, 013231, DOI: [10.1103/PhysRevResearch.4.013231](https://doi.org/10.1103/PhysRevResearch.4.013231) (2022). Publisher: American Physical Society.
38. Killoran, N. *et al.* Continuous-variable quantum neural networks. *Phys. Rev. Res.* **1**, 033063, DOI: [10.1103/PhysRevResearch.1.033063](https://doi.org/10.1103/PhysRevResearch.1.033063) (2019). Publisher: American Physical Society.
39. Mitarai, K., Negoro, M., Kitagawa, M. & Fujii, K. Quantum circuit learning. *Phys. Rev. A* **98**, 032309, DOI: [10.1103/PhysRevA.98.032309](https://doi.org/10.1103/PhysRevA.98.032309) (2018). Publisher: American Physical Society.
40. Larocca, M., Ju, N., García-Martín, D., Coles, P. J. & Cerezo, M. Theory of overparametrization in quantum neural networks. *Nat. Comput. Sci.* **3**, 542–551, DOI: [10.1038/s43588-023-00467-6](https://doi.org/10.1038/s43588-023-00467-6) (2023). Publisher: Nature Publishing Group.
41. Herrmann, J. *et al.* Realizing quantum convolutional neural networks on a superconducting quantum processor to recognize quantum phases. *Nat. Commun.* **13**, 4144, DOI: [10.1038/s41467-022-31679-5](https://doi.org/10.1038/s41467-022-31679-5) (2022). Publisher: Nature Publishing Group.
42. Beer, K. *et al.* Training deep quantum neural networks. *Nat. Commun.* **11**, 808, DOI: [10.1038/s41467-020-14454-2](https://doi.org/10.1038/s41467-020-14454-2) (2020). Publisher: Nature Publishing Group.
43. Abbas, A. *et al.* The power of quantum neural networks. *Nat. Comput. Sci.* **1**, 403–409, DOI: [10.1038/s43588-021-00084-1](https://doi.org/10.1038/s43588-021-00084-1) (2021). Publisher: Nature Publishing Group.
44. Hochreiter, S. & Schmidhuber, J. Long Short-Term Memory. *Neural Comput.* **9**, 1735–1780, DOI: [10.1162/neco.1997.9.8.1735](https://doi.org/10.1162/neco.1997.9.8.1735) (1997).
45. Schuster, M. & Paliwal, K. Bidirectional recurrent neural networks. *IEEE Transactions on Signal Process.* **45**, 2673–2681, DOI: [10.1109/78.650093](https://doi.org/10.1109/78.650093) (1997).
46. Graves, A., Mohamed, A.-r. & Hinton, G. Speech recognition with deep recurrent neural networks. In *2013 IEEE International Conference on Acoustics, Speech and Signal Processing*, 6645–6649, DOI: [10.1109/ICASSP.2013.6638947](https://doi.org/10.1109/ICASSP.2013.6638947) (2013). ISSN: 2379-190X.
47. Ronneberger, O., Fischer, P. & Brox, T. U-Net: Convolutional Networks for Biomedical Image Segmentation. In Navab, N., Hornegger, J., Wells, W. M. & Frangi, A. F. (eds.) *Medical Image Computing and Computer-Assisted Intervention – MICCAI 2015*, 234–241, DOI: [10.1007/978-3-319-24574-4\\_28](https://doi.org/10.1007/978-3-319-24574-4_28) (Springer International Publishing, Cham, 2015).



48. Bai, S., Kolter, J. Z. & Koltun, V. An Empirical Evaluation of Generic Convolutional and Recurrent Networks for Sequence Modeling, DOI: [10.48550/arXiv.1803.01271](https://doi.org/10.48550/arXiv.1803.01271) (2018). ArXiv:1803.01271 [cs].
49. Boström, H. crepes: a Python Package for Generating Conformal Regressors and Predictive Systems. In *Proceedings of the Eleventh Symposium on Conformal and Probabilistic Prediction with Applications*, 24–41 (PMLR, 2022). ISSN: 2640-3498.